

Superfluid extension of the self-consistent time-dependent band theory for neutron star matter: Anti-entrainment versus superfluid effects in the slab phase

Kenta Yoshimura^{1,*} and Kazuyuki Sekizawa^{1,2,3,†}

¹*Department of Physics, School of Science, Tokyo Institute of Technology, Tokyo 152-8551, Japan*

²*Nuclear Physics Division, Center for Computational Sciences, University of Tsukuba, Ibaraki 305-8577, Japan*

³*RIKEN Nishina Center, Saitama 351-0198, Japan*

(Dated: June 19, 2024)

Background: The inner crust of neutron stars consists of a Coulomb lattice of neutron-rich nuclei, immersed in a sea of superfluid neutrons with background relativistic electron gas. A proper quantum mechanical treatment for such a system under a periodic potential is the band theory of solids. The effect of band structure on the effective mass of dripped neutrons, the so-called *entrainment effect*, is currently in a debatable situation, and it has been highly desired to develop a microscopic nuclear band theory taking into account neutron superfluidity in a fully self-consistent manner.

Purpose: The main purpose of the present work is twofold: 1) to develop a formalism of the time-dependent self-consistent band theory, taking fully into account nuclear superfluidity, based on time-dependent density functional theory (TDDFT) extended for superfluid systems, and 2) to quantify the effects of band structure and superfluidity on the entrainment phenomenon, applying the formalism to the slab phase of the inner crust of neutron stars.

Methods: The fully self-consistent time-dependent band theory, proposed in a previous work [K. Sekizawa, S. Kobayashi, and M. Matsuo, *Phys. Rev. C* **105**, 045807 (2022)], is extended for superfluid systems. To this end, a superfluid TDDFT with a local treatment of pairing, known as time-dependent superfluid local density approximation (TDSLDA), is formulated in the coordinate space with a Skyrme-type energy density functional, adopting the Bloch's boundary condition. A real-time method is employed to extract the collective masses of a slab and of protons, which in turn quantify the conduction neutron number density and the neutron effective mass, i.e., the entrainment effect.

Results: Static calculations have been performed for a range of baryon number density ($n_b = 0.04\text{--}0.07\text{ fm}^{-3}$) under the β -equilibrium condition with and without superfluidity, for various inter-slab spacings. From the results, we find that the system gains energy through the formation of Cooper pairs for all densities examined, which supports the existence of superfluidity in the inner crust of cold neutron stars. From a response of the system to an external potential, we dynamically extract the collective masses of a slab and of protons immersed in neutron superfluid. The obtained results show the collective mass of a slab is substantially reduced by 57.5–82.5% for $n_b = 0.04\text{--}0.07\text{ fm}^{-3}$, which corresponds to an enhancement of conduction neutron number density and, thus, to a *reduction* of the neutron effective mass, which we call the *anti-entrainment* effect. A comparison of the results with and without superfluidity reveals that superfluidity slightly enhances the anti-entrainment effects for the slab phase of neutron-star matter. We discuss a novel phenomenon associated with superfluidity, that is, quasiparticle resonances in the inner crust, which are absent in normal systems.

Conclusions: Our fully self-consistent, microscopic, superfluid band theory calculations based on (TD)DFT showed that the effective mass of dripped neutrons is *reduced* by about 20–40% for $n_b = 0.04\text{--}0.07\text{ fm}^{-3}$ because of the band structure effects, and superfluidity slightly *enhances* the reduction.

I. INTRODUCTION

The band theory of solids, with the aid of Kohn-Sham density functional theory (DFT) [1–3], has become a standard tool in material science to understand and predict abundant properties of a wide variety of matters. Its time-dependent extension based on time-dependent DFT (TDDFT) [4–6] has also been extensively developed to explore electron dynamics under a strong laser field (see, e.g., Refs. [7–12] and references therein). Recently, the band theory of solids has been applied for studying properties of the inner crust of neutron stars [13–19], where nuclear bundles form crystalline structures, just in a similar way as terrestrial solids, which coexists with neutron superfluid and relativistic electron gas. Along the line with the previous work [19], this paper aims to develop a fully self-consistent, microscopic framework to describe structure and dynamics of the inner crust of neutron stars, taking fully into

account both the band structure and superfluid effects on the same footing.

The band theory of solids may not yet be a popular approach in the context of neutron-star studies. While a first indication of necessity of such a calculation was made in 1994 [20], realistic band theory calculations were achieved in 2005 for slab and rod phases [13], followed by three-dimensional (3D) calculations for Coulomb lattices of spherical nuclei [14, 17]. It has been shown that, based on band theory calculations on top of a nuclear potential obtained with the Thomas-Fermi-type approximation [21], the effective mass of dripped neutrons is increased by factors of 1.02–1.03 and 1.11–1.40 in the slab and rod phases, respectively. Furthermore, the 3D calculations showed that band structure effects always *enhance* the neutron effective mass and most strikingly in a certain low-density region ($0.02\text{ fm}^{-3} \lesssim n_b \lesssim 0.04\text{ fm}^{-3}$) it was found to be nearly 10 times or more larger than the bare neutron mass [17]. The increase of neutron effective mass is associated with the Bragg scattering of dripped neutrons off the periodic potential, which immobilize those otherwise-free neutrons. The latter effect is called the *entrainment effect*. The notable change

* yoshimura.k.ak@m.titech.ac.jp

† sekizawa@phys.titech.ac.jp

TABLE I. A summary of the complicated situation concerning the band structure effects in the inner crust of neutron stars. This work, with future extensions to 2D and 3D systems, aims to provide conclusive values of the neutron effective mass throughout the inner crust of neutron stars.

Author(s) (Year)	Dimension	Self-consistency	Superfluidity	m_n^*/m_n	n_b (fm $^{-3}$)	Ref.
Carter, Chamel & Haensel (2005)	1D	–	–	1.02–1.03	0.074–0.079	[13]
	2D	–	–	1.11–1.40	0.058–0.072	
Chamel (2005)	3D	–	–	1.07–15.4	0.03–0.086	[14]
Chamel (2012)	3D	–	–	1.21–13.6	0.0003–0.08	[17]
Kashiwaba & Nakatsukasa (2019)	1D	✓	–	0.65–0.75	0.07–0.08 [†]	[18]
Sekizawa, Kobayashi & Matsuo (2022)	1D	✓	–	0.59	0.04 [‡]	[19]
Yoshimura & Sekizawa (2024)	1D	✓	✓	0.58	0.07 [†]	This work
	2D, 3D	✓	✓	??	$\lesssim 0.07$	Future works

[†] Where appearance of the slab phase is expected.

[‡] With a fixed proton fraction, $Y_p = 0.1$.

of the neutron effective mass turned out to affect various interpretations of astrophysical phenomena of neutron stars such as pulsar glitches [23–25] and thermal as well as crustal properties [26–30], and it has attracted increasing interests over the years. (See, Ref. [22], for a review of band calculations of Chamel et al. and discussion on related topics.)

The situation regarding the band structure effects on dripped neutrons in the inner crust of neutron stars is still highly controversial (see Table I). While the band theory calculations assume a perfect crystalline structure, disorder of crystal may reduce the band structure effects [31]. Apart from the possible disorder effects, recently, fully self-consistent, microscopic band theory calculations based on DFT and its time-dependent extension (TDDFT) have been achieved for the slab phase of nuclear matter [18, 19]. In Refs. [18, 19], based on both static and dynamic calculations, respectively, the neutron effective mass was found to be *reduced* for the slab phase, which is called the *anti-entrainment* effects [19]. The latter observation is contradictory to the results of Ref. [13], which may be partly due to an improper definition of “free” neutron density for the slab and rod phases in the work of Carter et al. [13], as pointed out in Ref. [18]. Further applications of the fully self-consistent band theory to higher spatial dimensions have been highly desired.

However, in the aforementioned works, pairing correlations were neglected and it is not at all obvious how superfluidity affects the entrainment effect. In Ref. [32], it was argued, within the Bardeen-Cooper-Schrieffer (BCS) approximation, that pairing correlations do not affect much the results and the strong entrainment would remain. In later studies, pairing effects were studied for a 1D periodic potential within the BCS as well as Hartree-Fock-Bogoliubov (HFB) [also called Bogoliubov-de Gennes (BdG)] approximations, showing that the BCS treatment is not enough and a self-consistent treatment of pairing correlations is essentially important to correctly quantify the entrainment effect [33, 34]. However, none of those studies are fully self-consistent. In neutron-star matter, there is no “external” potential (except the gravitational one that is negligible in investigating nuclear-scale microphysics) and neutrons and protons are self-organizing to ar-

range a variety of crystalline structures. Therefore, it is an imperative task to develop a fully self-consistent microscopic framework that includes superfluidity to draw a clear conclusion on the magnitude of the entrainment effect.

In the present paper, before extending the framework of Ref. [19] to higher spatial dimensions, we shall first develop a formalism of fully self-consistent, microscopic time-dependent superfluid band calculations based on TDDFT for superfluid systems. According to the Hohenberg-Kohn theorem [1] with the Kohn-Sham scheme [2], DFT can, in principle, be an exact approach to quantum many-body problems. Its time-dependent extension [5, 6], based on the Runge-Gross theorem [4], allows us to describe complex non-linear dynamics as well as excited states. While (TD)DFT for superfluid (superconducting) systems was initially formulated with a non-local pair potential $\Delta(\mathbf{r}, \mathbf{r}')$ [37, 38], subsequent developments of its local treatment with a proper pairing renormalization scheme resulted in the so-called (time-dependent) superfluid local density approximation [(TD)SLDA] [39–43]. In the nuclear physics context, on the other side, (TD)DFT was originally developed as mean-field theories with effective nucleon-nucleon interactions, like the Skyrme (TD)HF approach [44–49]. Because of the historical reason, one may confuse (TD)SLDA as (TD)HFB with a zero-range effective pairing interaction. We note, however, that the pairing renormalization scheme [40, 41] makes the theory cutoff independent, if it is taken to be sufficiently large, and allows one to work with a local pairing field $\Delta(\mathbf{r})$ within a well-defined theoretical framework. Thus, in the same way as one regards Skyrme (TD)HF as (TD)DFT, we can regard Skyrme (TD)HFB with a zero-range pairing interaction as superfluid (TD)DFT, if such a proper pairing renormalization scheme is adopted. TDSLDA [35, 53] has been successfully applied not only for nuclear systems [50–54], but also for cold-atomic systems [55–60]. In this work, we develop a fully self-consistent (time-dependent) superfluid band theory based on (TD)SLDA, imposing the Bloch’s boundary condition to quasiparticle wave functions, which corresponds to an extension of the previous work [19] for superfluid systems. By applying the formalism to the slab phase of neutron-star matter

under the β -equilibrium condition, we demonstrate the validity of our formalism and shed new light on the role of superfluidity in the entrainment phenomenon.

The article is organized as follows. In Sec. II, we explain detailed formalisms of the self-consistent time-dependent superfluid band theory for the inner crust of neutron stars, and provide computational details in Sec. III. In Sec. IV, we present the results of band theory calculations for the slab phase of nuclear matter under the β -equilibrium condition. In Sec. V, conclusions and prospect are given.

II. FORMULATION

A. The HFB theory

1. The matrix representation

Let us first succinctly recapitulate the general framework of the HFB theory, clarifying our notations. Here we start with a generic Hamiltonian in the second quantization form,

$$\hat{H} = \sum_{kl} t_{kl} \hat{a}_k^\dagger \hat{a}_l + \frac{1}{4} \sum_{klmn} \bar{v}_{klmn} \hat{a}_k^\dagger \hat{a}_l^\dagger \hat{a}_n \hat{a}_m, \quad (1)$$

where \hat{a}_k and \hat{a}_k^\dagger are particle annihilation and creation operators, respectively, that obey the Fermionic anticommutation relations: i.e., $\{\hat{a}_k, \hat{a}_l^\dagger\} = \delta_{kl}$ and $\{\hat{a}_k, \hat{a}_l\} = \{\hat{a}_k^\dagger, \hat{a}_l^\dagger\} = 0$. t_{kl} and \bar{v}_{klmn} ($\equiv v_{klmn} - v_{klnm}$) are usual matrix elements of a one-body kinetic energy operator and of a two-body interaction, respectively, where the latter one is antisymmetrized for convenience. In the HFB theory, quasiparticle annihilation and creation operators, $\hat{\beta}_\mu$ and $\hat{\beta}_\mu^\dagger$, respectively, are introduced via the Bogoliubov transformation of \hat{a}_k and \hat{a}_k^\dagger :

$$\begin{pmatrix} \hat{\beta} \\ \hat{\beta}^\dagger \end{pmatrix} = \mathcal{W}^\dagger \begin{pmatrix} \hat{a} \\ \hat{a}^\dagger \end{pmatrix}. \quad (2)$$

Here we have introduced column vectors, $\hat{\beta} \equiv (\hat{\beta}_1, \hat{\beta}_2, \dots, \hat{\beta}_M)^\top$, $\hat{\beta}^\dagger \equiv (\hat{\beta}_1^\dagger, \hat{\beta}_2^\dagger, \dots, \hat{\beta}_M^\dagger)^\top$, $\hat{a} \equiv (\hat{a}_1, \hat{a}_2, \dots, \hat{a}_M)^\top$, and $\hat{a}^\dagger \equiv (\hat{a}_1^\dagger, \hat{a}_2^\dagger, \dots, \hat{a}_M^\dagger)^\top$, to simplify the notation, where M corresponds to the dimension of basis states. The $2M \times 2M$ Bogoliubov transformation matrix \mathcal{W} can be written as

$$\mathcal{W} = \begin{pmatrix} U & V^* \\ V & U^* \end{pmatrix}, \quad (3)$$

where U and V are $M \times M$ matrices. The Bogoliubov transformation matrix is unitary, i.e. $\mathcal{W}^\dagger \mathcal{W} = \mathcal{W} \mathcal{W}^\dagger = I_{2M}$, with I_{2M} being a $2M$ -dimensional identity matrix. The latter property ensures that $\hat{\beta}_\mu$ and $\hat{\beta}_\mu^\dagger$ also obey the Fermionic anticommutation relations. One can write down explicitly the quasiparticle annihilation and creation operators, respectively, as

follows:

$$\hat{\beta}_\mu = \sum_i \left(U_{i\mu}^* \hat{a}_i + V_{i\mu}^* \hat{a}_i^\dagger \right), \quad (4)$$

$$\hat{\beta}_\mu^\dagger = \sum_i \left(U_{i\mu} \hat{a}_i^\dagger + V_{i\mu} \hat{a}_i \right). \quad (5)$$

Note that we use Greek indices (such as μ, ν, \dots) for labeling positive-energy quasiparticle states, while Roman indices (such as i, j, \dots) are used for labeling single-particle states, except some obvious cases.

The HFB state, the trial many-body wave function for a variation, is defined as a vacuum of quasiparticles, i.e. $\hat{\beta}_\mu | \text{HFB} \rangle = 0$ for all μ . Based on the variational principle, one can derive the well-known HFB equation:

$$\begin{pmatrix} h - \lambda I_M & \Delta \\ -\Delta^* & -h^* + \lambda I_M \end{pmatrix} \begin{pmatrix} U_\mu \\ V_\mu \end{pmatrix} = E_\mu \begin{pmatrix} U_\mu \\ V_\mu \end{pmatrix}, \quad (6)$$

where $h = t + \Gamma$ denotes the single-particle Hamiltonian matrix with a matrix for the mean-field potential Γ , Δ is a matrix for the pair potential, λ is the chemical potential, and U_μ and V_μ represent the μ -th column of the U and V matrices, respectively. The (k, l) component of the mean-field potential and the pair potential matrices are defined, respectively, as follows:

$$\Gamma_{kl} = \sum_{mn} \bar{v}_{kmln} \rho_{nm}, \quad (7)$$

$$\Delta_{kl} = \frac{1}{2} \sum_{mn} \bar{v}_{klmn} \kappa_{mn}. \quad (8)$$

Here the one-body density matrix, ρ , and the pairing tensor, κ , are, respectively, given by

$$\rho_{kl} = \langle \hat{a}_l^\dagger \hat{a}_k \rangle = (V^* V^\top)_{kl}, \quad (9)$$

$$\kappa_{kl} = \langle \hat{a}_l \hat{a}_k \rangle = (V^* U^\top)_{kl}, \quad (10)$$

where the brackets, $\langle \dots \rangle$, represent an expectation value in the HFB state. This is the usual matrix representation of the HFB theory. By definition, ρ is hermitian ($\rho^\dagger = \rho$) and κ is skew symmetric ($\kappa^\top = -\kappa$).

2. Treatment of a system with certain symmetries in the coordinate-space representation

Next, let us consider a case where a system possesses certain symmetries, and introduce the coordinate-space representation of the HFB theory. The formulas given here are actually useful to formulate the superfluid band theory with the Bloch's boundary condition in Sec. II B. When a system possesses symmetries, the Hamiltonian commutes with operators associated with the corresponding symmetric transformations and there are conserved quantities with which one can classify quantum states. For instance, for a system with the spherical symmetry, the orbital angular momentum L and its projection m are conserved, being good quantum numbers. In such a

case, states with different values of (L, m) are not mixed, and the Hamiltonian matrix can be arranged to have a block diagonal form. In the following we shall denote such a set of arbitrary good quantum numbers as Ω .

Since single- and quasi-particle states can be classified according to the set of quantum numbers, Ω , we may explicitly indicate it as $\mu \rightarrow \{\nu \Omega\}$ and $i \rightarrow \{j \Omega\}$. For a system with symmetries, the quasiparticle annihilation and creation operators, Eqs. (4) and (5), respectively, can be written as

$$\hat{\beta}_{\nu\Omega} = \sum_j \left(U_{j\Omega, \nu\Omega}^* \hat{a}_{j\Omega} + V_{j\bar{\Omega}, \nu\Omega}^* \hat{a}_{j\bar{\Omega}}^\dagger \right), \quad (11)$$

$$\hat{\beta}_{\nu\Omega}^\dagger = \sum_j \left(U_{j\Omega, \nu\Omega} \hat{a}_{j\Omega}^\dagger + V_{j\bar{\Omega}, \nu\Omega} \hat{a}_{j\bar{\Omega}} \right). \quad (12)$$

Note that $\bar{\Omega}$, which appeared as a subscript of the second term in the parentheses in Eqs. (11) and (12), stands for the same set of quantum numbers as Ω , but any ‘‘countable’’ quantum numbers involved in it have opposite sign [e.g., for the case of $\Omega = (L, m)$, $\bar{\Omega} = (L, -m)$]. It is simply because a ‘‘hole’’ of a state with countable quantum number(s) could be characterized like a particle which has the opposite sign for the countable quantum number(s). In this way, the quantum numbers in the left- and right-hand-side of Eqs. (11) and (12) are being consistent. It should be noted that Eqs. (11) and (12) mean the original U, V matrices are now in a block diagonal form. That is, U relates single- and quasi-particle states with the same Ω , while V relates those with Ω and $\bar{\Omega}$, being $U_{j\Omega, \nu\Omega'} = U_{j\Omega, \nu\Omega} \delta_{\Omega\Omega'}$ and $V_{j\bar{\Omega}, \nu\Omega'} = V_{j\bar{\Omega}, \nu\bar{\Omega}} \delta_{\bar{\Omega}\bar{\Omega}'}$.

To obtain the coordinate-space representation with the spin degree of freedom, let us introduce the field operators,

$$\hat{\psi}(\mathbf{r}\sigma) = \sum_{j\Omega} \phi_{j\Omega}(\mathbf{r}\sigma) \hat{a}_{j\Omega}, \quad (13)$$

$$\hat{\psi}^\dagger(\mathbf{r}\sigma) = \sum_{j\Omega} \phi_{j\Omega}^*(\mathbf{r}\sigma) \hat{a}_{j\Omega}^\dagger. \quad (14)$$

Note that the summation is taken over all single-particle states ($i = \{j \Omega\}$), by definition. Here $\phi_{j\Omega}(\mathbf{r}\sigma) \equiv \langle \mathbf{r}\sigma | j\Omega \rangle = \langle \mathbf{r}\sigma | \hat{a}_{j\Omega}^\dagger | 0 \rangle$ denotes the single-particle wave function, where

$|0\rangle$ is the vacuum state. The field operator creates a particle with spin σ ($=\uparrow$ or \downarrow) at a position \mathbf{r} in the vacuum, i.e. $|\mathbf{r}\sigma\rangle = \hat{\psi}^\dagger(\mathbf{r}\sigma)|0\rangle$. Using the orthonormal properties of the single-particle wave functions, $\langle \phi_k | \phi_l \rangle \equiv \sum_\sigma \int \phi_k^*(\mathbf{r}\sigma) \phi_l(\mathbf{r}\sigma) d\mathbf{r} = \delta_{kl}$, with Eqs. (13) and (14), the particle annihilation and creation operators can be represented, respectively, as follows:

$$\hat{a}_{j\Omega} = \sum_\sigma \int \phi_{j\Omega}^*(\mathbf{r}\sigma) \hat{\psi}(\mathbf{r}\sigma) d\mathbf{r}, \quad (15)$$

$$\hat{a}_{j\Omega}^\dagger = \sum_\sigma \int \phi_{j\Omega}(\mathbf{r}\sigma) \hat{\psi}^\dagger(\mathbf{r}\sigma) d\mathbf{r}. \quad (16)$$

Substituting Eqs. (15) and (16) into Eqs. (11) and (12), one finds

$$\hat{\beta}_{\nu\Omega} = \sum_\sigma \int \left(u_{\nu\Omega}^*(\mathbf{r}\sigma) \hat{\psi}(\mathbf{r}\sigma) + v_{\nu\Omega}^*(\mathbf{r}\sigma) \hat{\psi}^\dagger(\mathbf{r}\sigma) \right) d\mathbf{r}, \quad (17)$$

$$\hat{\beta}_{\nu\Omega}^\dagger = \sum_\sigma \int \left(u_{\nu\Omega}(\mathbf{r}\sigma) \hat{\psi}^\dagger(\mathbf{r}\sigma) + v_{\nu\Omega}(\mathbf{r}\sigma) \hat{\psi}(\mathbf{r}\sigma) \right) d\mathbf{r}, \quad (18)$$

where

$$u_{\nu\Omega}(\mathbf{r}\sigma) \equiv \sum_j U_{j\Omega, \nu\Omega} \phi_{j\Omega}(\mathbf{r}\sigma), \quad (19)$$

$$v_{\nu\Omega}(\mathbf{r}\sigma) \equiv \sum_j V_{j\bar{\Omega}, \nu\Omega} \phi_{j\bar{\Omega}}^*(\mathbf{r}\sigma). \quad (20)$$

Those are the coordinate-space representation of the u and v components of the quasiparticle wave functions. The quasiparticle wave functions are normalized to be

$$\sum_\sigma \int \left[|u_{\nu\Omega}(\mathbf{r}\sigma)|^2 + |v_{\nu\Omega}(\mathbf{r}\sigma)|^2 \right] d\mathbf{r} = 1. \quad (21)$$

In the same way as in the matrix representation, a variational calculation leads to the corresponding coordinate-space representation of the HFB equation:

$$\int d\mathbf{r}' \begin{pmatrix} \hat{h}_{\uparrow\uparrow}(\mathbf{r}, \mathbf{r}') - \lambda \delta_{\mathbf{r}, \mathbf{r}'} & \hat{h}_{\uparrow\downarrow}(\mathbf{r}, \mathbf{r}') & 0 & \Delta(\mathbf{r}, \mathbf{r}') \\ \hat{h}_{\downarrow\uparrow}(\mathbf{r}, \mathbf{r}') & \hat{h}_{\downarrow\downarrow}(\mathbf{r}, \mathbf{r}') - \lambda \delta_{\mathbf{r}, \mathbf{r}'} & -\Delta(\mathbf{r}, \mathbf{r}') & 0 \\ 0 & -\Delta^*(\mathbf{r}, \mathbf{r}') & -\hat{h}_{\uparrow\uparrow}^*(\mathbf{r}, \mathbf{r}') + \lambda \delta_{\mathbf{r}, \mathbf{r}'} & -\hat{h}_{\downarrow\downarrow}^*(\mathbf{r}, \mathbf{r}') \\ \Delta^*(\mathbf{r}, \mathbf{r}') & 0 & -\hat{h}_{\uparrow\uparrow}^*(\mathbf{r}, \mathbf{r}') & -\hat{h}_{\downarrow\downarrow}^*(\mathbf{r}, \mathbf{r}') + \lambda \delta_{\mathbf{r}, \mathbf{r}'} \end{pmatrix} \begin{pmatrix} u_{\nu\Omega}(\mathbf{r}'\uparrow) \\ u_{\nu\Omega}(\mathbf{r}'\downarrow) \\ v_{\nu\Omega}(\mathbf{r}'\uparrow) \\ v_{\nu\Omega}(\mathbf{r}'\downarrow) \end{pmatrix} = E_{\nu\Omega} \begin{pmatrix} u_{\nu\Omega}(\mathbf{r}\uparrow) \\ u_{\nu\Omega}(\mathbf{r}\downarrow) \\ v_{\nu\Omega}(\mathbf{r}\uparrow) \\ v_{\nu\Omega}(\mathbf{r}\downarrow) \end{pmatrix} \quad (22)$$

where $\delta_{\mathbf{r}, \mathbf{r}'} \equiv \delta(\mathbf{r} - \mathbf{r}')$. In the coordinate-space representation, the number and anomalous densities are defined as $n(\mathbf{r}) \equiv \sum_\sigma n(\mathbf{r}\sigma, \mathbf{r}\sigma)$ and $\kappa(\mathbf{r}, \mathbf{r}') \equiv \kappa(\mathbf{r}\uparrow, \mathbf{r}'\downarrow)$, respec-

tively, where

$$\begin{aligned} n(\mathbf{r}\sigma, \mathbf{r}'\sigma') &\equiv \langle \hat{\psi}^\dagger(\mathbf{r}'\sigma') \hat{\psi}(\mathbf{r}\sigma) \rangle \\ &= \sum_{i\Omega_1 j\Omega_2 \nu\Omega} \phi_{i\Omega_1}^*(\mathbf{r}'\sigma') \phi_{j\Omega_2}(\mathbf{r}\sigma) V_{j\Omega_2, \nu\Omega}^* V_{\nu\Omega, i\Omega_1}^\dagger \\ &= \sum_{\nu\Omega} v_{\nu\Omega}^*(\mathbf{r}\sigma) v_{\nu\Omega}(\mathbf{r}'\sigma'), \end{aligned} \quad (23)$$

$$\begin{aligned}
\kappa(\mathbf{r}\sigma, \mathbf{r}'\sigma') &\equiv \langle \hat{\psi}(\mathbf{r}'\sigma') \hat{\psi}(\mathbf{r}\sigma) \rangle \\
&= \sum_{i\Omega_1 j\Omega_2 \nu\Omega} \phi_{i\Omega_1}(\mathbf{r}'\sigma') \phi_{j\Omega_2}(\mathbf{r}\sigma) V_{j\Omega_2, \nu\Omega}^* U_{\nu\Omega, i\Omega_1}^T \\
&= \sum_{\nu\Omega} v_{\nu\Omega}^*(\mathbf{r}\sigma) u_{\nu\Omega}(\mathbf{r}'\sigma'). \tag{24}
\end{aligned}$$

When the single-particle Hamiltonian contains no terms that mix spin states (i.e. $\hat{h}_{\uparrow\downarrow} = \hat{h}_{\downarrow\uparrow} = 0$), the HFB equation (22) can be decomposed into two equations with a half of the original dimension as

$$\begin{aligned}
\int d\mathbf{r}' \begin{pmatrix} \hat{h}(\mathbf{r}, \mathbf{r}') - \lambda\delta_{\mathbf{r}, \mathbf{r}'} & \Delta(\mathbf{r}, \mathbf{r}') \\ \Delta^*(\mathbf{r}, \mathbf{r}') & -\hat{h}^*(\mathbf{r}, \mathbf{r}') + \lambda\delta_{\mathbf{r}, \mathbf{r}'} \end{pmatrix} \begin{pmatrix} u_{\nu\Omega}(\mathbf{r}'\uparrow) \\ v_{\nu\Omega}(\mathbf{r}'\downarrow) \end{pmatrix} \\
= E_{\nu\Omega} \begin{pmatrix} u_{\nu\Omega}(\mathbf{r}\uparrow) \\ v_{\nu\Omega}(\mathbf{r}\downarrow) \end{pmatrix}, \tag{25}
\end{aligned}$$

where $\hat{h} = \hat{h}_{\uparrow\uparrow} = \hat{h}_{\downarrow\downarrow}$. From a diagonalization of the HFB matrix, one obtains not only the quasiparticle states, but also the quasihole states with negative eigenvalues, $-E_{\nu\Omega}$. Thanks to this so-called quasiparticle-quasihole symmetry, the other spin component of quasiparticle wave functions, i.e. $(v_{\nu\Omega}^*(\mathbf{r}\uparrow), u_{\nu\Omega}^*(\mathbf{r}\downarrow))^T$ for $-E_{\nu\Omega}$, can be found in the negative energy states.

B. Superfluid band theory with a Skyrme-type EDF

1. The Bloch's boundary condition

In this section, we formulate the band theory of solids for superfluid systems. What one has to do is to combine the Bloch's boundary condition with the HFB framework. The essence of the band theory is to impose the periodicity of the crystal to the wave functions of the system. According to the Floquet-Bloch theorem, it can be achieved, representing the single-particle wave functions by modulated plane waves [61],

$$\phi_{j\mathbf{k}}^{(q)}(\mathbf{r}\sigma) = \frac{1}{\sqrt{\mathcal{V}}} \tilde{\phi}_{j\mathbf{k}}^{(q)}(\mathbf{r}\sigma) e^{i\mathbf{k}\cdot\mathbf{r}}, \tag{26}$$

where \mathcal{V} stands for the volume of a unit cell and \mathbf{k} is the Bloch wave vector. In this section, we explicitly indicate the isospin degree of freedom by an index q , where $q = n$ for neutrons and $q = p$ for protons. The periodicity of the system is then encoded into the function $\tilde{\phi}_{j\mathbf{k}}^{(q)}(\mathbf{r}\sigma)$ as

$$\tilde{\phi}_{j\mathbf{k}}^{(q)}(\mathbf{r} + \mathbf{T}, \sigma) = \tilde{\phi}_{j\mathbf{k}}^{(q)}(\mathbf{r}\sigma), \tag{27}$$

where \mathbf{T} is the lattice translation vector. We will refer to the dimensionless function $\tilde{\phi}_{j\mathbf{k}}^{(q)}(\mathbf{r}\sigma)$ as a Bloch wave function.

If the potential is local in space, there is no correlation between unit cells and the Hamiltonian can be written in a block diagonal form. It is thus possible to regard the Bloch wave vector \mathbf{k} as a sort of quantum numbers associated with a translational symmetry in a broad sense. That is, we can regard the

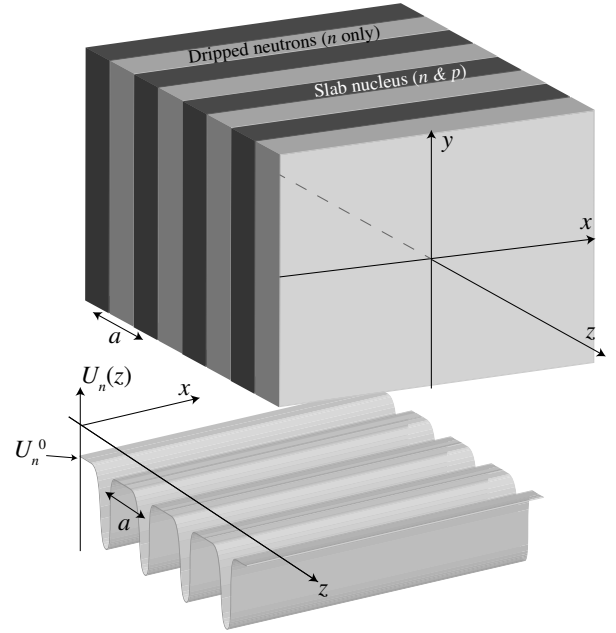


FIG. 1. Schematic picture showing the geometry of the systems under study. The nuclear slabs extend parallel to xy plane and are aligned with a period a along z direction, as depicted in the upper part of the figure. In the lower part, the nuclear mean-field potential is depicted in xz plane. Note that when dripped neutrons exist the maximum value of the mean field potential for neutrons (U_n^0 in the picture) is negative, even outside the slabs. The figure has been reprinted from Ref. [18] with permission.

Bloch wave vectors \mathbf{k} and $\bar{\mathbf{k}} (= -\mathbf{k})$ as the countable quantum numbers Ω and $\bar{\Omega}$, respectively, which were introduced in Sec. II A 2. We note that the form of single-particle wave functions is the same for $\tilde{\phi}_{j\bar{\mathbf{k}}}^{(q)}(\mathbf{r}\sigma)$, meaning that the sign of the exponent is different for $\tilde{\phi}_{j\bar{\mathbf{k}}}^{(q)}$ because of the relation, $\bar{\mathbf{k}} = -\mathbf{k}$. By substituting Eq. (26) into Eqs. (19) and (20), we find that the quasiparticle wave functions, $u_{\nu\mathbf{k}}(\mathbf{r}\sigma)$ and $v_{\nu\mathbf{k}}(\mathbf{r}\sigma)$, can be written as follows:

$$u_{\nu\mathbf{k}}^{(q)}(\mathbf{r}\sigma) = \frac{1}{\sqrt{\mathcal{V}}} \tilde{u}_{\nu\mathbf{k}}^{(q)}(\mathbf{r}\sigma) e^{i\mathbf{k}\cdot\mathbf{r}}, \tag{28}$$

$$v_{\nu\mathbf{k}}^{(q)}(\mathbf{r}\sigma) = \frac{1}{\sqrt{\mathcal{V}}} \tilde{v}_{\nu\mathbf{k}}^{(q)}(\mathbf{r}\sigma) e^{i\mathbf{k}\cdot\mathbf{r}}, \tag{29}$$

where $\tilde{u}_{\nu\mathbf{k}}^{(q)}(\mathbf{r} + \mathbf{T}, \sigma) = \tilde{u}_{\nu\mathbf{k}}^{(q)}(\mathbf{r}\sigma)$ and $\tilde{v}_{\nu\mathbf{k}}^{(q)}(\mathbf{r} + \mathbf{T}, \sigma) = \tilde{v}_{\nu\mathbf{k}}^{(q)}(\mathbf{r}\sigma)$ hold. Notice that the sign of the exponent is the same for both u and v components. It is an important key to formulate the superfluid band theory as shown in the subsequent sections.

In the present paper, we consider 1-dimensional (1D) crystalline structure, i.e. the slab (or “lasagna”) phase of nuclear matter, where slabs are extending parallel to xy plane and are in a periodic sequence along z direction; See Fig. 1. In this case the lattice vector \mathbf{T} reads

$$\mathbf{T} = T_x \hat{e}_x + T_y \hat{e}_y + a n_z \hat{e}_z, \tag{30}$$

where T_x and T_y are arbitrary real numbers, n_z is an integer,

a denotes the period of (or distance between) the neighboring slabs, and \hat{e}_i is the unit vector along the i ($= x, y$, or z) direction. Since the single-particle wave functions along the x and y directions are solely the plane waves, the Bloch's boundary condition, Eq. (27), is now reduced to

$$\tilde{\phi}_{j\mathbf{k}}^{(q)}(z+a, \sigma) = \tilde{\phi}_{j\mathbf{k}}^{(q)}(z\sigma). \quad (31)$$

That is, the Bloch wave functions have 1D spatial dependence:

$$u_{\nu\mathbf{k}}^{(q)}(\mathbf{r}\sigma) = \frac{1}{\sqrt{\mathcal{V}}} \tilde{u}_{\nu\mathbf{k}}^{(q)}(z\sigma) e^{i\mathbf{k}\cdot\mathbf{r}}, \quad (32)$$

$$v_{\nu\mathbf{k}}^{(q)}(\mathbf{r}\sigma) = \frac{1}{\sqrt{\mathcal{V}}} \tilde{v}_{\nu\mathbf{k}}^{(q)}(z\sigma) e^{i\mathbf{k}\cdot\mathbf{r}}. \quad (33)$$

The z component of the Bloch wave vector can be reduced within the first Brillouin zone, $-\pi/a \leq k_z \leq \pi/a$. In practical calculations, we discretize the first Brillouin zone into N_{k_z} points, i.e. $\Delta k_z = \frac{2\pi}{a} \frac{1}{N_{k_z}}$. This implementation corresponds to a calculation with a length $\mathcal{L} \equiv aN_{k_z}$ with the ordinary periodic boundary condition. Thus, the normalization condition (21) now reads

$$\mathcal{A} \sum_{\sigma} \int_0^{\mathcal{L}} \left[|u_{\nu\mathbf{k}}^{(q)}(\mathbf{r}\sigma)|^2 + |v_{\nu\mathbf{k}}^{(q)}(\mathbf{r}\sigma)|^2 \right] dz = 1, \quad (34)$$

where \mathcal{A} stands for the normalization area such that $\mathcal{V} = \mathcal{L}\mathcal{A}$. Because of the periodicity of the quasiparticle wave functions, Eq. (34) is equivalent to

$$\sum_{\sigma} \int_0^a \left[|\tilde{u}_{\nu\mathbf{k}}^{(q)}(z\sigma)|^2 + |\tilde{v}_{\nu\mathbf{k}}^{(q)}(z\sigma)|^2 \right] dz = a. \quad (35)$$

2. Energy density functionals

The main ingredient of DFT is the EDF. In this work, the EDF used is almost the same as given in the previous work [19], except the introduction of a pairing functional. For completeness, here we briefly recall the equations, because some of them require a caution specific to the superfluid systems.

The total energy per nucleon of the system is given by

$$\frac{E_{\text{tot}}}{A} = \frac{1}{N_b} \int_0^a (\mathcal{E}_{\text{nucl}}(z) + \mathcal{E}_e(z)) dz, \quad (36)$$

where $\mathcal{E}_{\text{nucl}}$ denotes a nuclear part of the energy density and \mathcal{E}_e is the electron's one. Here, $N_b = N_n + N_p$ [The subscript 'b' stands for 'baryons' (which are nucleons, in the present study)], where $N_q = \int_0^a n_q(z) dz$ is the total number of neutrons ($q = n$) or protons ($q = p$) per unit area within a single period a , with $n_q(z)$ being the number density of neutrons ($q = n$) or protons ($q = p$). The nuclear energy density is given as a sum of kinetic, nuclear (interaction), and pairing energy densities,

$$\mathcal{E}_{\text{nucl}}(z) = \mathcal{E}_{\text{kin}}(z) + \mathcal{E}_{\text{Sky}}(z) + \mathcal{E}_{\text{pair}}(z), \quad (37)$$

where

$$\mathcal{E}_{\text{kin}}(z) = \sum_{q=n,p} \frac{\hbar^2}{2m_q} \tau_q(z), \quad (38)$$

$$\mathcal{E}_{\text{Sky}}(z) = \sum_{t=0,1} \left[C_t^{\rho} [n_0] n_t^2(z) + C_t^{\Delta\rho} n_t(z) \partial_z^2 n_t(z) + C_t^{\tau} (n_t(z) \tau_t(z) - \mathbf{j}_t^2(z)) \right], \quad (39)$$

$$\mathcal{E}_{\text{pair}}(z) = - \sum_{q=n,p} \Delta_q(z) \kappa_q^*(z), \quad (40)$$

where m_q is the nucleon mass¹ and ∂_z represents a spatial derivative with respect to the z coordinate. In this work, we develop a formalism for a widely-used Skyrme-type EDF for the nuclear part. The kinetic and momentum densities in \mathcal{E}_{Sky} (39) are formally defined, respectively, by

$$\tau_q(\mathbf{r}) = (\nabla \cdot \nabla') n_q(\mathbf{r}, \mathbf{r}') \Big|_{\mathbf{r}=\mathbf{r}'}, \quad (41)$$

$$\mathbf{j}_q(\mathbf{r}) = \text{Im}[(\nabla - \nabla') n_q(\mathbf{r}, \mathbf{r}') \Big|_{\mathbf{r}=\mathbf{r}'}, \quad (42)$$

where ∇ and ∇' act on the spatial coordinates \mathbf{r} and \mathbf{r}' , respectively. The time-odd momentum densities vanish in static calculations, while they are, in general, finite in a dynamic situation. The subscript t in Eq. (39) specifies isoscalar ($t = 0$) and isovector ($t = 1$) densities, which are defined, for the number density for instance, by $n_0(z) = n_n(z) + n_p(z)$ and $n_1(z) = n_n(z) - n_p(z)$, respectively (the subscript 0 is often omitted). The detailed expressions of the coefficients by means of Skyrme force parameters can be found in, e.g., Eq. (A1) in Ref. [67] (where symbols A_t^X were used instead of C_t^X here, where X stands for ρ, τ , and $\Delta\rho$). $C_t^{\rho} [n_0]$ depends on the local number density as $C_t^{\rho} [n_0] = C_t^{\rho} + C_{t,D}^{\rho} n_0^{\delta}(z)$ as in Ref. [68].

To evaluate the densities, Eqs. (23), (24), (41), and (42), we need to take summations over all positive-energy quasiparticle states $\mu = \{\nu \mathbf{k}\}$. For the slab phase under study, the summation over k_x and k_y can be replaced with integrals, $\sum_{k_x, k_y} \rightarrow \int \mathcal{A} dk_x dk_y / (2\pi)^2 = \int \mathcal{A} k_{\parallel} dk_{\parallel} / (2\pi)$, where $k_{\parallel} \equiv (k_x^2 + k_y^2)^{1/2}$ is the magnitude of the Bloch wave vector parallel to the slabs [19]. Then, the various densities can be

¹ In this work, $m_n = 939.56542052 \text{ MeV}/c^2$ and $m_p = 938.27208816 \text{ MeV}/c^2$ are used, as in Ref. [19].

written as follows:

$$n_q(z) = \sum_{\nu k_z \sigma} \int \frac{k_{\parallel} dk_{\parallel}}{2\pi\mathcal{L}} |v_{\nu\mathbf{k}}^{(q)}(z\sigma)|^2, \quad (43)$$

$$\tau_q(z) = \sum_{\nu k_z \sigma} \int \frac{k_{\parallel} dk_{\parallel}}{2\pi\mathcal{L}} \left[k_{\parallel}^2 |v_{\nu\mathbf{k}}^{(q)}(z\sigma)|^2 + |(\partial_z + ik_z)v_{\nu\mathbf{k}}^{(q)}(z\sigma)|^2 \right], \quad (44)$$

$$\mathbf{j}_q(z) = - \sum_{\nu k_z \sigma} \int \frac{k_{\parallel} dk_{\parallel}}{2\pi\mathcal{L}} \times \text{Im} \left[v_{\nu\mathbf{k}}^{(q)*}(z\sigma)(\partial_z + ik_z)v_{\nu\mathbf{k}}^{(q)}(z\sigma) \right] \hat{e}_z, \quad (45)$$

$$\kappa_q(z) = \sum_{\nu k_z} \int \frac{k_{\parallel} dk_{\parallel}}{2\pi\mathcal{L}} v_{\nu\mathbf{k}}^{(q)*}(z\uparrow)u_{\nu\mathbf{k}}^{(q)}(z\downarrow). \quad (46)$$

Note that a minus sign appears in the current density (45), due to the definition (20) that relates $v_{\nu\Omega}(\mathbf{r}\sigma)$ and $\phi_{j\bar{\Omega}}^*(\mathbf{r}\sigma)$.

The pairing part of EDF, $\mathcal{E}_{\text{pair}}$ (40), contains the pairing field $\Delta_q(z)$ which is given by

$$\Delta_q(z) = -g_{q,\text{eff}}(z)\kappa_q(z), \quad (47)$$

where $g_{q,\text{eff}}(z)$ in Eq. (47) is an effective pairing coupling constant [41], which is calculated as follows [81]:

$$\frac{1}{g_{q,\text{eff}}(z)} = \frac{1}{g_0} - \frac{m_q^{\oplus}(z)\pi}{4\pi^2\hbar^2 a} K, \quad (48)$$

where g_0 is the bare coupling constant, $m_q^{\oplus}(z)$ is a ‘‘microscopic’’ effective mass, which will be defined in Eq. (55), and K is a numerical constant that corresponds to the integral,

$$\begin{aligned} K &= \frac{12}{\pi} \int_0^{\frac{\pi}{2}} \ln(1 + 1/\cos^2\theta) d\theta \\ &= 2.442749607806335 \dots \end{aligned} \quad (49)$$

We set the bare coupling constant to $g_0 = 200 \text{ MeV fm}^3$ in the present work. This value has been used for finite nuclei in the literature [82–84]. We find that this coupling constant yields a reasonable value of the pairing field for neutron-star matter on the order of 1 MeV [cf. Fig. 4(b)]. In the present work, we thus employ this coupling constant for the sake of simplicity. It is to mention that there exist several refined treatments of the coupling constant that correctly reproduce density dependence of the neutron pairing gap in neutron star matter (see, e.g., Refs. [85, 86])

The Coulomb part of EDF reads

$$\mathcal{E}_{\text{Coul}}^{(p)}(z) = \frac{1}{2}n_p(z)V_{\text{Coul}}(z) - \frac{3e^2}{4} \left(\frac{3}{\pi} \right)^{1/3} n_p^{4/3}(z), \quad (50)$$

where $V_{\text{Coul}}(z)$ denotes the Coulomb potential for protons and e is the elementary charge. The Slater approximation has been adopted for the Coulomb exchange functional. For the Coulomb potential, we solve the Poisson equation,

$$\frac{d^2}{dz^2} V_{\text{Coul}}(z) = -\frac{e^2}{\varepsilon_0} n_{\text{ch}}(\mathbf{r}), \quad (51)$$

where ε_0 is the vacuum permittivity. Here, $n_{\text{ch}}(z) \equiv n_p(z) - n_e$ denotes the charge density, neglecting the charge form factor of protons. Electrons are assumed to be uniformly distributed with the density $n_e = \bar{n}_p$, where $\bar{n}_q = \frac{1}{a} \int_0^a n_q(z) dz$ is the average nucleon number density. The Coulomb potential is subjected to the charge neutrality condition, $\int_0^a V_{\text{Coul}}(z) dz = 0$.

For the electron’s EDF, $\mathcal{E}_e(z)$ in Eq. (36), we use formulas for a relativistic electron gas. For explicit expressions, We refer readers to Refs. [18, 19].

3. Skyrme (TD)SLDA equations for the slab phase

From an appropriate functional derivative, one can derive the corresponding single-particle Hamiltonian which enters the (TD)SLDA equation. Because our working EDFs are local in space, the resulting equation becomes also a local one. In the same way as the normal (without pairing correlations) self-consistent band theory [19], the point is that an operation of a spatial derivative on a quasiparticle wave function (32) generates an additional \mathbf{k} -dependent term as follows:

$$\nabla u_{\nu\mathbf{k}}^{(q)}(\mathbf{r}\sigma) = \frac{1}{\sqrt{V}} e^{i\mathbf{k}\cdot\mathbf{r}} (\partial_z \hat{e}_z + i\mathbf{k}) \tilde{u}_{\nu\mathbf{k}}^{(q)}(z\sigma), \quad (52)$$

where the same is true also for the v component (33). Substituting Eqs. (32) and (33) into a localized version of Eq. (25), and factoring out the common function $e^{i\mathbf{k}\cdot\mathbf{r}}$ after operations of the spatial derivatives, we obtain

$$\begin{pmatrix} \hat{h}^{(q)}(z) + \hat{h}_{\mathbf{k}}^{(q)}(z) - \lambda_q & \Delta_q(z) \\ \Delta_q^*(z) & -\hat{h}^{(q)*}(z) - \hat{h}_{-\mathbf{k}}^{(q)*}(z) + \lambda_q \end{pmatrix} \times \begin{pmatrix} \tilde{u}_{\nu\mathbf{k}}^{(q)}(z\uparrow) \\ \tilde{v}_{\nu\mathbf{k}}^{(q)}(z\downarrow) \end{pmatrix} = E_{\nu\mathbf{k}} \begin{pmatrix} \tilde{u}_{\nu\mathbf{k}}^{(q)}(z\uparrow) \\ \tilde{v}_{\nu\mathbf{k}}^{(q)}(z\downarrow) \end{pmatrix}. \quad (53)$$

It should be noted that, while we deal with a three-dimensional system, the equations to be solved are essentially one-dimensional ones, significantly reducing the computational cost.

The single-particle Hamiltonian, $\hat{h}^{(q)}(z)$, is given by

$$\begin{aligned} \hat{h}^{(q)}(z) &= -\nabla \cdot M^{(q)}(z)\nabla + U^{(q)}(z) \\ &+ \frac{1}{2i} \left[\nabla \cdot \mathbf{I}^{(q)}(z) + \mathbf{I}^{(q)}(z) \cdot \nabla \right]. \end{aligned} \quad (54)$$

Note that the differential operators in Eq. (54) act on all spatial functions located right side of them. Here, we have introduced a time-even mean-field $M^{(q)}(z)$ defined as

$$M^{(q)}(z) \equiv \frac{\hbar^2}{2m_q^{\oplus}(z)} = \frac{\hbar^2}{2m_q} + \sum_{q'=n,p} C_{q'}^{\tau(q)} n_{q'}(z), \quad (55)$$

where $m_q^{\oplus}(z)$ is the ‘‘microscopic’’ effective mass which should be distinguished from a ‘‘macroscopic’’ one discussed

in Sec. IV D. $U^{(q)}(z)$ and $I^{(q)}(z)$ are time-even and time-odd mean field potentials, respectively, defined as

$$\begin{aligned}
U^{(q)}(z) = & \sum_{q'=n,p} \left[2C_{q'}^{\rho(q)} n_{q'}(z) + 2C_{q'}^{\nabla\rho(q)} \partial_z^2 n_{q'}(z) \right. \\
& + C_{q'}^{\tau(q)} \tau_{q'}(z) + 2n_0^\alpha(z) C_{q'D}^{\rho(q)} n_{q'}(z) \left. \right] \\
& + \alpha n_0^{\alpha-1}(z) \sum_{t=0,1} C_{tD}^\rho n_t^2(z) \\
& + U_{\text{Coul}}(z) \delta_{qp} \\
& + \sum_{q'=n,p} \frac{\partial g_{q',\text{eff}}}{\partial n_q} |\kappa_{q'}(z)|^2, \tag{56}
\end{aligned}$$

$$I^{(q)}(z) = -2 \sum_{q'=n,p} C_{q'}^{\tau(q)} \mathbf{j}_{q'}(z), \tag{57}$$

where

$$U_{\text{Coul}}(z) = V_{\text{Coul}}(z) - e^2 \left(\frac{3}{\pi} \right)^{1/3} n_p^{1/3}(z). \tag{58}$$

Note that there is an additional contribution to $U^{(q)}(z)$ arising from the density derivative of the effective pairing coupling constant, which is given by

$$\frac{\partial g_{q',\text{eff}}}{\partial n_q} = [g_{q',\text{eff}}(z)]^2 \frac{K}{8\pi a} \left(\frac{\hbar^2}{2m_q^\oplus(z)} \right)^{-2} C_q^{\tau(q')}. \tag{59}$$

Following the previous work [19], we have defined a shorthand notation,

$$C_n^{\text{X}(q)} \equiv C_0^{\text{X}} + \eta_q C_1^{\text{X}}, \tag{60}$$

$$C_p^{\text{X}(q)} \equiv C_0^{\text{X}} - \eta_q C_1^{\text{X}}, \tag{61}$$

where X stands for the superscript of the coefficients, i.e., ρ , τ , or $\Delta\rho$, and $\eta_q = +1$ (-1) for neutrons (protons). We note that the time-odd potential vanishes in a static situation. The single-particle Hamiltonian which depends on the Bloch wave vector, $\hat{h}_{\mathbf{k}}^{(q)}(z)$, can be represented as follows [19]:

$$\hat{h}_{\mathbf{k}}^{(q)}(z) = \frac{\hbar^2 \mathbf{k}^2}{2m_q^\oplus(z)} + \hbar \mathbf{k} \cdot \hat{\mathbf{v}}^{(q)}(z), \tag{62}$$

where $\hat{\mathbf{v}}^{(q)}(z)$ is the so-called velocity operator,

$$\begin{aligned}
\hat{\mathbf{v}}^{(q)}(z) &= \frac{1}{i\hbar} \left[\mathbf{r}, \hat{h}^{(q)}(z) \right] \\
&= -i\hbar \left(\nabla \frac{1}{2m_q^\oplus(z)} + \frac{1}{2m_q^\oplus(z)} \nabla \right) + \frac{1}{\hbar} \mathbf{I}_q(z). \tag{63}
\end{aligned}$$

As will be described in Sec. IV D, we apply the real-time method, proposed in Ref. [19], where we extract the collective masses of a slab and of protons from a dynamic response of the system to an external force. The external force can be introduced by means of a time-dependent, uniform vector potential $A_z(t)$ that couples only with protons which are localized inside slabs. Such a vector potential is equivalent to a

uniform electric field, $E_z(t) = -(1/c)dA_z(t)/dt$. Time evolution of the system is described by the TDSLDA equation in the velocity gauge [19]:

$$\begin{aligned}
& \begin{pmatrix} \hat{h}^{(q)}(z, t) + \hat{h}_{\mathbf{k}(t)}^{(q)}(z, t) & \Delta_q(z, t) \\ \Delta_q^*(z, t) & -\hat{h}^{(q)*}(z, t) - \hat{h}_{-\mathbf{k}(t)}^{(q)*}(z, t) \end{pmatrix} \\
& \times \begin{pmatrix} \tilde{u}_{\nu\mathbf{k}}^{(q)}(z\uparrow, t) \\ \tilde{v}_{\nu\mathbf{k}}^{(q)}(z\downarrow, t) \end{pmatrix} = i\hbar \frac{\partial}{\partial t} \begin{pmatrix} \tilde{u}_{\nu\mathbf{k}}^{(q)}(z\uparrow, t) \\ \tilde{v}_{\nu\mathbf{k}}^{(q)}(z\downarrow, t) \end{pmatrix}, \tag{64}
\end{aligned}$$

where the prime on the quasiparticle wave functions indicates that they are represented in the velocity gauge,

$$\tilde{u}_{\nu\mathbf{k}}^{(q)}(z, t) \equiv \exp \left[-\frac{ie}{\hbar c} A_z(t) z \right] \tilde{u}_{\nu\mathbf{k}}^{(q)}(z, t), \tag{65}$$

and a similar formula (with the opposite sign in the exponent) holds for the v components (33). Notice that the Bloch wave vector in the \mathbf{k} -dependent single-particle Hamiltonian (62) in Eq. (64) is shifted as a function of time, according to the following relation:

$$\mathbf{k}(t) = \mathbf{k} + \frac{e}{\hbar c} A_z(t) \hat{\mathbf{e}}_z. \tag{66}$$

All densities can be expressed in terms of the quasiparticle wave functions in the velocity gauge, replacing $\tilde{u}_{\nu\mathbf{k}}^{(q)} \rightarrow \tilde{u}_{\nu\mathbf{k}}^{(q)}$, $\tilde{v}_{\nu\mathbf{k}}^{(q)} \rightarrow \tilde{v}_{\nu\mathbf{k}}^{(q)}$, and $k_z \rightarrow k_z(t)$. More detailed explanations on the expressions in the velocity gauge can be found in Ref. [19].

III. COMPUTATIONAL DETAILS

We have newly developed a parallel computational code from scratch that reproduces all the results presented in Ref. [19] and extended it to include superfluidity. All the calculations were carried out with Skyrme SLy4 EDF [69] as in Ref. [19]. We consider a situation where nuclear slabs extend along xy directions, forming a perfect crystalline structure along z axis with a period a . We discretize the z coordinate into a uniform grid with spacing Δz to represent quasiparticle wave functions. The mesh spacing is set to $\Delta z = 0.5$ fm. The spectral method with fast Fourier transformations (FFTs) are used to evaluate the first and second spacial derivatives. The Poisson equation for the Coulomb potential is solved also with the FFT algorithm. We discretize the first Brillouin zone $-\pi/a \leq k_z \leq \pi/a$ into N_{k_z} points. We use $N_{k_z} = 80$ as in Ref. [19]. For the Bloch wave vector parallel to the slabs, k_{\parallel} , we introduce a cutoff $k_{\parallel}^{\text{max}}$ and discretize it with a Δk_{\parallel} step. For the calculations presented in this paper, $k_{\parallel}^{\text{max}} = 1.5 \text{ fm}^{-1}$ and $\Delta k_{\parallel} = 0.01 \text{ fm}^{-1}$ are adopted. We have confirmed that these computational settings provide satisfactory convergent results for the systems under study.

For time evolution, we use the eighth-order Taylor expansion method with a single predictor-corrector step with $\Delta t = 0.1 \text{ fm}/c$. With this setting, we have confirmed that the total number of nucleons and the total energy per nucleon are conserved with 10^{-6} - and 10^{-10} -MeV accuracy, respectively,

within the simulation time of 4,000 fm/c. For the extraction of the collective mass of a slab, we dynamically introduce an external potential for protons, $E_z(t) = S(\eta, w, t)E_z$, as a function of time t , where

$$S(\eta, w, t) = \frac{1}{2} + \frac{1}{2} \tanh \left[\eta \tan \left(\frac{\pi t}{w} - \frac{\pi}{2} \right) \right] \quad (67)$$

is a switching function which varies smoothly from 0 to 1 within an interval $t = [0, w]$. In this way we can avoid unnecessary excitations of the system [19]. In the present paper, $\eta = 1$ and $w = 2,000$ fm/c were used and calculations were continued up to $t = 4,000$ fm/c. We set the strength of the external potential as $eE_z = 10^{-3}$ MeV/fm, as in Ref. [19].

The slab period a under study is about $a \approx 30$ fm and, thus, the number of grid points along the z coordinate is $N_z \approx 60$. In such a case, the total number of quasiparticle wave functions that need to be solved in the current computational setup is estimated to be

$$\begin{aligned} N_z \times N_{k_z} \times N_{k_{\parallel}} \times 2 \text{ (isospin)} \times 2 \text{ (} u \text{ and } v) \\ = 60 \times 80 \times 150 \times 4 = 2,880,000. \end{aligned}$$

That is, although 1D equations look easily tractable, one has to deal with millions of complex, non-linear, partial differential equations for the quasiparticle wave functions. Note that if the single-particle Hamiltonian involves a term that mixes spins the number increases by a factor of two, because of an explicit treatment for the spin degree of freedom. Currently, our code is parallelized with respect to the Bloch wave number k_z using the message passing interface (MPI).

IV. RESULTS AND DISCUSSION

A. On the convergence of self-consistent calculations

To solve the static SLDA equation, we performed iterative diagonalizations of the Hamiltonian matrix. At every step m , the chemical potentials for neutrons and protons λ_q were updated to obtain correct neutron and proton numbers satisfying the β -equilibrium condition. To this end, we adjust the chemical potential of protons as $\lambda_p^{(m+1)} = \lambda_p^{(m)} - \alpha_\lambda (N_b^{(m+1)} - N_b^{(0)})$ with $\alpha_\lambda = 50$, where $N_b^{(0)}$ denotes the requested nucleon number, i.e., $N_b^{(0)} = an_b$. While, the chemical potential of neutrons are determined simply through the β -equilibrium condition, $\mu_n = \mu_p + \mu_e$. From the calculations, we realized that a use of the modified Broyden's method (see, e.g., Ref. [70] and references therein) is crucial to get a convergent result with a reasonable computational time. The modified Broyden mixing was applied to the mean-field, pairing, and chemical potentials so that the unitarity of the Bogoliubov transformation matrix is always preserved [70]. The Broyden vector thus reads $\mathbf{V} = \{M^{(n)}(z), M^{(p)}(z), U^{(n)}(z), U^{(p)}(z), \text{Re}[\Delta_n(z)], \text{Im}[\Delta_n(z)], \text{Re}[\Delta_p(z)], \text{Im}[\Delta_p(z)], \mu_n, \mu_p\}$, i.e., with $8N_z + 2$ dimensions. The modified Broyden's method also contains a parameter α that controls a rate of mixing, which we set $\alpha = 0.1$.

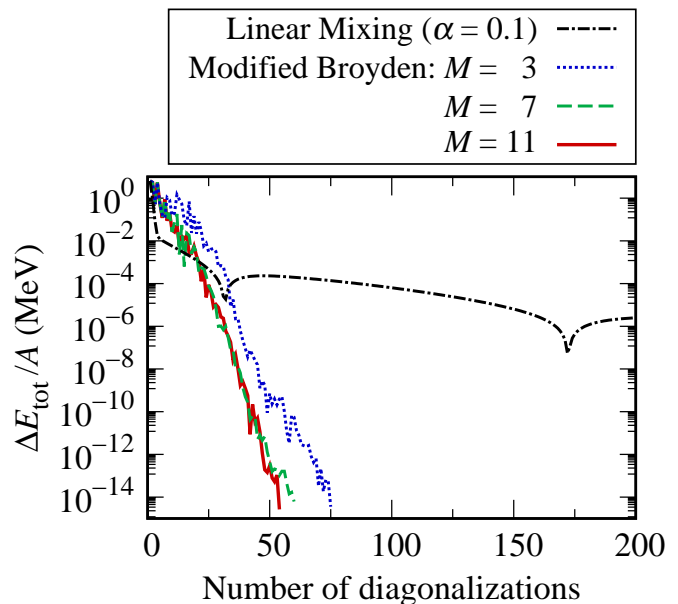


FIG. 2. The change of the total energy per nucleon between two successive iterations, $\Delta E_{\text{tot}}/A = |E_{\text{tot}}^{(m)} - E_{\text{tot}}^{(m-1)}|/A$, is plotted as a function of the number of diagonalizations m for the system with $n_b = 0.05$ fm $^{-3}$ under the β -equilibrium condition. The results obtained with the modified Broyden's method with $M = 11, 7$, and 3 are shown by solid, dashed, and dotted lines, respectively. The result obtained with the linear mixing method with $\alpha = 0.1$ is also shown by a dot-dashed line for comparison.

As a typical example, we show in Fig. 2 change in total energy per nucleon, $\Delta E_{\text{tot}}/A \equiv |E_{\text{tot}}^{(m)} - E_{\text{tot}}^{(m-1)}|/A$, as a function of the number of diagonalizations for $n_b = 0.05$ fm $^{-3}$ under the β -equilibrium condition. In the modified Broyden's method, information of M previous steps is used for updating the Broyden vector. For comparison, results with $M = 11, 7$, and 3 are shown by solid, dashed, and dotted lines, respectively. A result obtained with a simple linear mixing is also presented by a dash-dotted line. In the linear mixing method, potentials were updated simply according to $X^{(m+1)} = (1 - \alpha)X^{(m)} + \alpha X'^{(m+1)}$ with $\alpha = 0.1$, where $X'^{(m+1)}$ stands here for a tentative potential obtained after the $(m + 1)$ th diagonalization of the Hamiltonian matrix. From the figure, one finds that the linear mixing may be good for the first 10–20 iterations, but its convergence is very slow, which cannot reach $\Delta E < 10^{-6}$ MeV even after 200 diagonalizations. One may naively expect that the convergence would be improved by increasing the rate of mixing, however, we found that the calculation becomes unstable already for $\alpha = 0.15$. In contrast, we find a good convergent behavior with the modified Broyden's method, where the energy change decreases exponentially down to 10^{-14} MeV. In the present paper, we use $M = 7$ and set a convergence criterion as $\Delta E_{\text{tot}}/A < 10^{-10}$ MeV.

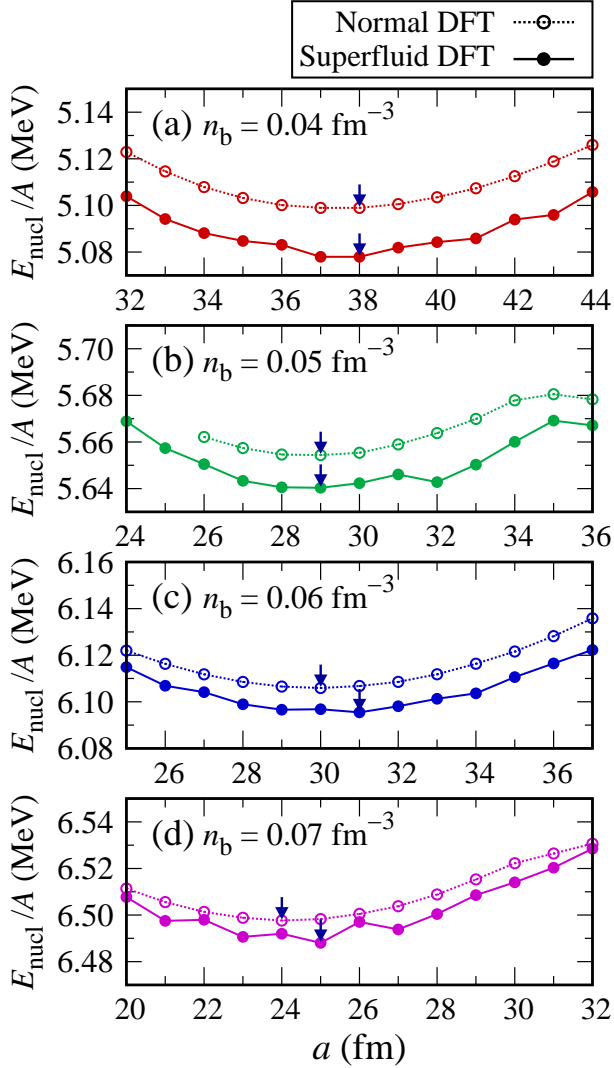


FIG. 3. Nuclear energy per nucleon, E_{nucl}/A , is shown as a function of the slab period a . Results for $n_b = 0.04, 0.05, 0.06$, and 0.07 fm^{-3} are exhibited in panels (a), (b), (c), and (d), respectively. In each panel, results of superfluid band calculations are shown by filled circles connected with solid lines, while those without superfluidity are represented by open circles connected with dotted lines. The minimum energy locations are indicated by arrows.

B. On the optimal slab period

In self-consistent band theory calculations, the slab period a is linked to the size of the computational region, $N_z \Delta z$. Therefore, to figure out the optimal slab period that minimizes the total energy of the system, we need to repeat static calculations by changing the number of lattice points, N_z .

To show how the energy depends on the slab period a , we show in Fig. 3 the nuclear energy per nucleon, i.e. $E_{\text{nucl}} \equiv \frac{1}{N_b} \int_0^a \mathcal{E}_{\text{nucl}}(z) dz$, as a function of the slab period a for $n_b = 0.04, 0.05, 0.06$, and 0.07 fm^{-3} under the β -equilibrium condition. The results of superfluid band theory calculations are shown by solid circles connected with solid lines, while those of normal band theory (without pairing correlations) are

TABLE II. A summary of self-consistent superfluid band theory calculations for a range of baryon number densities $n_b = 0.04\text{--}0.07 \text{ fm}^{-3}$ under the β -equilibrium condition. From the left to right columns, the baryon number density, n_b , in fm^{-3} , proton fraction, Y_p , optimal slab period, a , in fm, background neutron number density, n_n^{bg} , in fm^{-3} , and average absolute values of the pairing field, $\overline{\Delta}_q$ ($q = n$ for neutrons and $q = p$ for protons), in MeV, are presented.

n_b	Y_p	a	n_n^{bg}	$\overline{\Delta}_n$	$\overline{\Delta}_p$
0.04	3.31×10^{-2}	38	3.23×10^{-2}	1.20	9.34×10^{-2}
0.05	3.30×10^{-2}	29	4.08×10^{-2}	1.34	6.88×10^{-2}
0.06	3.37×10^{-2}	31	4.96×10^{-2}	1.49	8.33×10^{-2}
0.07	3.50×10^{-2}	25	5.80×10^{-2}	1.55	2.25×10^{-2}

shown by open circles connected with dotted lines. From the figure, we find that the total energy is always lower with superfluidity, gaining energy through the pairing correlations, as expected for the inner crust of neutron stars. In addition, a parabolic behavior is visible, which is associated with balance between Coulomb and nuclear interactions. While a too small slab period is energetically unfavorable due to the Coulomb repulsion, a too large value results in loss of nuclear attraction. In the figure, the optimal slab period that minimizes the total energy is indicated by an arrow. It is visible from Figs. 3(c) and 3(d) that inclusion of superfluidity could slightly affect the period a .

It should be noted that the energy curve shows somewhat different behavior when one includes electrons' contribution. Namely, the total energy per nucleon, E_{tot}/A , exhibits a gentle dependence on the slab period a with smaller curvature, and the resulting optimal slab period tends to be larger than those shown in Fig. 3 (see Appendix A for details). It is, of course, desirable to optimize the slab period a by minimizing the total energy of the system. In the present work, however, we analyze the systems that minimize the nuclear energy, following Ref. [18], because the primary purpose of this study is to quantify the effects of band structure and superfluidity for systems with different baryon number densities. In the future works, where we extend the theoretical framework to deal with 2D and 3D crystalline structures and make a quantitative prediction on the neutron effective mass, configurations that minimize the total energy should be investigated.

C. Static properties and band structure

The results of fully self-consistent superfluid band theory calculations are summarized in Table. II. In the table, we show the proton fraction, Y_p , which is determined by the β -equilibrium condition, the optimal slab period, a , the background neutron number density, n_n^{bg} , and the average absolute value of the pairing field, $\overline{\Delta}_q$. Clearly, the system is quite neutron-rich, with proton fractions around 0.033–0.035. As baryon number density increases, the optimal slab period a decreases, as expected. In our calculations, a nuclear slab is located at the center of the computational region, $z = a/2$,

and the background neutron number density is defined as $n_n^{\text{bg}} = n_n(0) = n_n(a)$. The background neutron number density n_n^{bg} increases with density, indicating that more neutrons are dripped outside of the slab for higher densities. The average absolute values of the pairing field is defined by

$$\bar{\Delta}_q = \frac{1}{N_q} \int_0^a |\Delta_q(z)| n_q(z) dz. \quad (68)$$

In the present computational settings, both neutrons and protons are found to be in the superfluid and superconducting phases, respectively, although the average proton pairing gap is very small, as compared to the neutron's one.

In Fig. 4, we show a typical density distribution (a) and the absolute value of the pairing field (b) for the system with $n_b = 0.05 \text{ fm}^{-3}$ under the β -equilibrium condition. Because of the small proton fraction $Y_p = 0.033$, there are substantial portion of dripped neutrons outside of the slab, whose density distribution looks quite diffusive (or “melting,” close to the uniform nuclear matter). This characteristic is more pronounced in the case of distribution of the pairing field. The absolute value of the pairing field is much larger for neutrons, but protons are also superconducting although $\bar{\Delta}_p$ is small. Since substantial amount of neutrons are dripped outside of the slab, we can expect the formation of band structure. Now, a question arises: how the superfluidity affects the band structure?

Figure 5 shows the quasiparticle energies $E_{\nu\mathbf{k}}^{(q)}$ for the system with $n_b = 0.05 \text{ fm}^{-3}$ under the β -equilibrium condition, as an illustrative example. In Fig. 5(a), the results are plotted as a function of the Bloch wave number k_z within the first Brillouin zone, $-\pi/a \leq k_z \leq \pi/a$, with $k_{\parallel} = 0$, while quasiparticle energies for $k_z > 0$ are plotted as a function of k_{\parallel} in Fig. 5(b). Line color changes gradually according to the ascending order of $E_{\nu\mathbf{k}}^{(n)}$, just to guide the eye. One should keep in mind that quasiparticle energies are related to single-particle ones in the canonical basis as

$$E_{\mu} = \pm \sqrt{(\varepsilon_{\mu} - \lambda)^2 + \Delta^2}. \quad (69)$$

From Fig. 5(a), deep-hole states which are within the potential well, $\varepsilon_{\mu} < U_n^0$, can be seen as horizontal lines above 30 MeV^2 . In the figure, many other lines are visible, showing k_z dependence, which are associated with dripped neutrons that extend spatially outside the slabs. In Fig. 5(b), on the other hand, we find there are parabolic curves, some of which are convex upward and the rest is opposite. Basically, k_{\parallel} dependence originates from $\hbar^2 k_{\parallel}^2 / (2m_q^{\oplus})$ in Eq. (62) and, thus, those curves which are convex upward are contributions solely from states below the chemical potential. Clearly, quasiparticle energies exhibit complex dependence on the Bloch wave vector \mathbf{k} , which we call the band structure. We will discuss the corresponding single-particle energies in Sec. IV E (cf. Fig. 10).

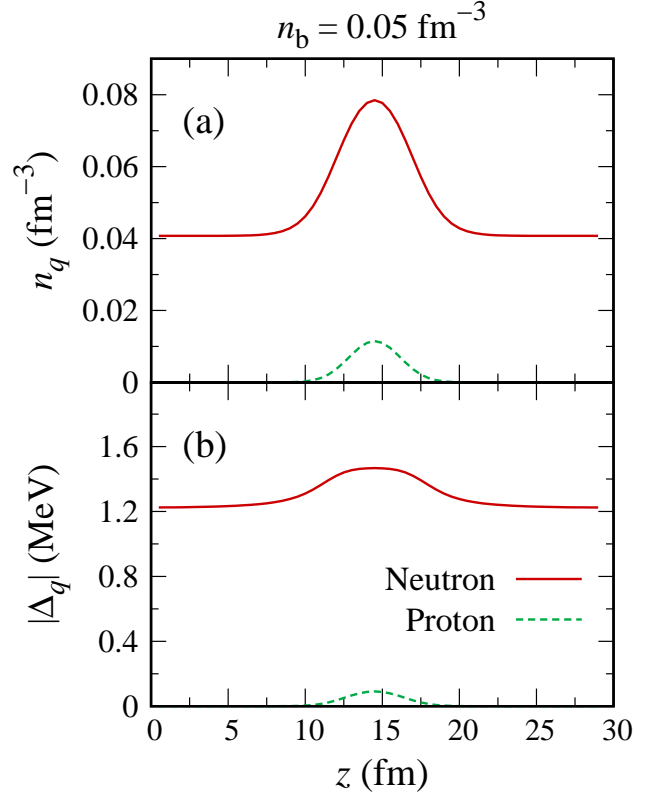


FIG. 4. Nucleon number densities, $n_q(z)$, and the absolute value of the pairing field, $|\Delta_q(z)|$, for the system with $n_b = 0.05 \text{ fm}^{-3}$ under the β -equilibrium condition are shown in panels (a) and (b), respectively, as a function of z coordinate. Solid lines show those of neutrons, while dashed lines show those of protons.

D. Anti-entrainment effects

1. Real-time method

In this section, we present results of fully self-consistent time-dependent simulations to quantify the entrainment effects in the slab phase of neutron-star matter in the presence of superfluidity. We employ a real-time method that enables us to extract the collective masses of a slab and of protons from a dynamic response of the system to an external force, the method proposed in Ref. [19]. Here we succinctly digest the essence of the approach, referring readers to Ref. [19] for details.

In the inner crust of neutron stars, where dripped superfluid neutrons permeate a crystalline structure of nuclear bundles, it is not at all obvious how to distinguish bound and unbound (free) neutrons. One may naively subtract background uniform neutron density to define density of a cluster as a “bump” in the whole density distribution, or compare depth of a mean-field potential and single-particle energies to count the number of neutrons within the potential well [77]. In real situations, however, due to the self-organizing character of neutron-star matter, i.e. there is no clear-cut separation between clusters and the others, those are served only as a naive estimation. In addition, part of dripped neutrons are expected to be immo-

² U_n^0 denotes the maximum value of the mean-field potential, which takes negative values even outside of the slabs when dripped neutrons exist (cf. Fig. 1).

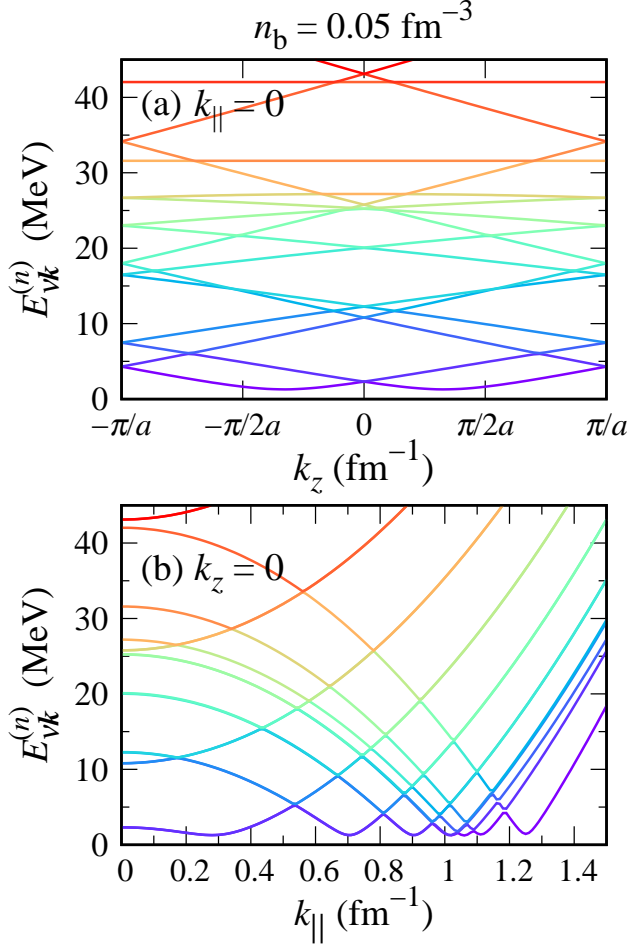


FIG. 5. Quasiparticle energies of neutrons, $E_{\nu k}^{(n)}$, are shown as functions of k_z for $k_{\parallel} = 0$ (a) and as functions of k_{\parallel} for $k_z = 0$ (b) for the system with $n_b = 0.05 \text{ fm}^{-3}$ under the β -equilibrium condition. Line color changes gradually according to the ascending order of $E_{\nu k}^{(n)}$, just to guide the eye.

bilized or trapped by the periodic structure through the Bragg scattering. This is the so-called entrainment effect and the amount of the “effectively-bound” neutrons is the matter of debate. We note, moreover, that superfluidity may also affect the collective mass of nuclear clusters [62]. It is thus a quite complicated problem and only fully self-consistent superfluid band calculations developed here can provide conclusive results.

The real-time method [19] offers an intuitive approach to extract the collective mass of a nuclear cluster immersed in neutron superfluid. In the latter approach, we exert an external force F_{ext} on protons which are well localized inside the cluster. The protons together with effectively bound (bound plus entrained) neutrons start moving towards the direction of the external force. If the force is constant and there are no redundant excitations other than the collective translational motion, the cluster would exhibit a constant acceleration motion, $F_{\text{ext}} = \dot{P} = M_{\text{cluster}} a_p$, where \dot{P} is time derivative of the total linear momentum of the system, M_{cluster} and a_p are the collective mass and the acceleration of the cluster, respectively.

Since protons are localized in space, the center-of-mass position of protons, $Z_p(t) = \frac{1}{N_p} \int_0^a z n_p(z) dz$, is a well defined quantity. Thus, we can numerically compute the acceleration of the cluster, $a_p(t) = d^2 Z_p / dt^2$. Adopting the classical relation, we can evaluate the collective mass of the cluster as well as that of protons (per unit area) as follows:

$$M_{\text{cluster}} = \frac{\dot{P}_{\text{tot}}}{a_p}, \quad (70)$$

$$M_p = \frac{\dot{P}_p}{a_p}, \quad (71)$$

where $P_{\text{tot}} = P_n + P_p$ is the total linear momentum and P_q is the linear momentum of neutrons ($q = n$) and protons ($q = p$),

$$P_q(t) = \hbar \int_0^a j_z^{(q)}(z, t) dz. \quad (72)$$

Since we have both the collective masses of the cluster and of protons, we can define the collective mass of effectively-bound neutrons per unit area by

$$M_n^{\text{eff. bound}} = M_{\text{cluster}} - M_p. \quad (73)$$

The number density of conduction neutrons which can freely conduct can be quantified as follows:

$$n_n^c = \frac{N_n - N_n^{\text{eff. bound}}}{a}, \quad (74)$$

where $N_n^{\text{eff. bound}} = M_n^{\text{eff. bound}} / m_{n, \text{bg}}^{\oplus}$ is the average number of the effectively-bound neutrons per unit area, where $m_{n, \text{bg}}^{\oplus} = m_n^{\oplus} [n_n^{\text{bg}}]$. We note that the microscopic effective mass becomes equivalent to the bare mass for $n_n^{\text{bg}} = 0$, and the equation is valid for isolated slabs without dripped neutrons. Having the conduction neutron number density, n_n^c , we can quantify the “macroscopic” effective mass, m_n^* , as follows:

$$\frac{m_n^*}{m_{n, \text{bg}}^{\oplus}} = \frac{n_n^f}{n_n^c}, \quad (75)$$

where n_n^f denotes the (energetically) free neutron number density, which is the counter part of the energetically-bound neutrons. In this way, we can extract the macroscopic effective mass from a dynamic response of the system to the external potential. The real-time method outlined above can be directly applied also for the superfluid TDDFT, where all complex effects are automatically included in the description in a fully self-consistent manner.

2. The main results

In Fig. 6, we show obtained acceleration of protons, $a_p(t)$, in panel (a), time-derivative of the total linear momentum, $\dot{P}_{\text{tot}}(t)$, in panel (b), and that of the proton linear momentum, $\dot{P}_p(t)$, in panel (c), as a function of time. Results obtained with superfluidity is shown by solid lines, while those obtained without superfluidity are shown by dotted lines. From

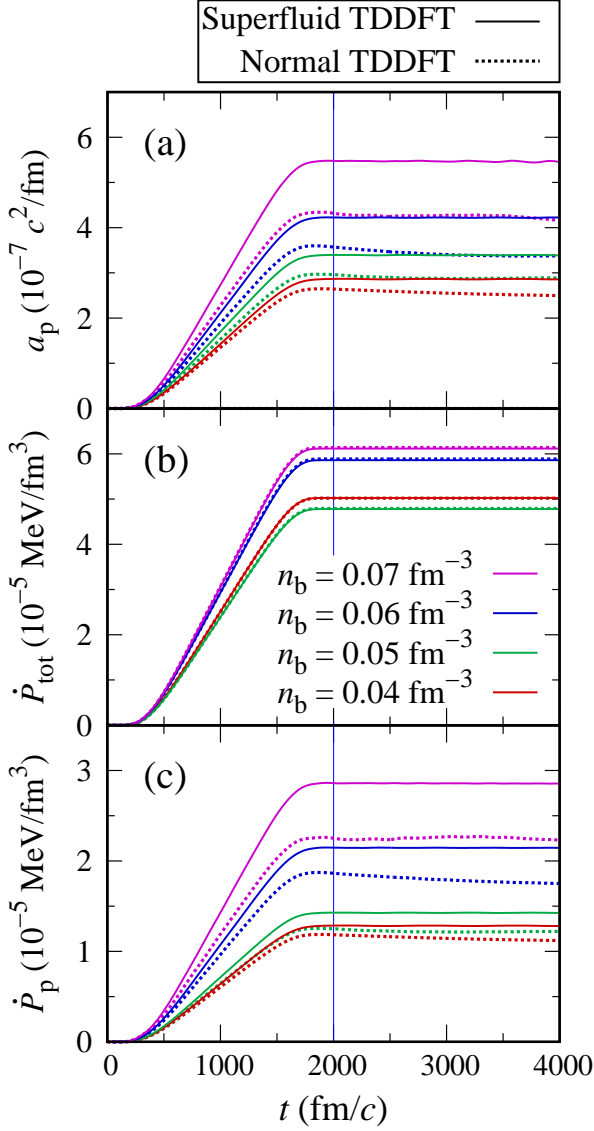


FIG. 6. Results of fully self-consistent time-dependent band calculations for various baryon number densities, $n_b = 0.04\text{--}0.07\text{ fm}^{-3}$, under the β -equilibrium condition. Results obtained with (without) superfluidity are shown by solid (dotted) lines. In panels (a), (b), and (c), the acceleration of the center-of-mass position of protons, a_p , the rate of change of the total linear momentum, \dot{P}_{tot} , and the rate of change of the proton linear momentum, \dot{P}_p , are presented, respectively. The vertical line indicates the time up to which the external force is turned on.

$t = 0$ to $2,000\text{ fm}/c$, we smoothly switch on the external potential and it is kept constant for $t \geq 2,000\text{ fm}/c$. As a result, we observe that all those quantities become almost constant for $t \geq 2,000\text{ fm}/c$, as expected. It is to be mentioned that the acceleration is more stably constant for the superfluid case (solid lines), as compared with the normal one (dotted lines). As is shown in Fig. 6(b), the classical relation, $F_{\text{ext}} = \dot{P}_{\text{tot}}$ holds nicely, in both cases with and without superfluidity. From Figs. 6(a) and (c), we find that both a_p and \dot{P}_p tend to be larger when we include the superfluidity. It indicates that the collective mass of the slab is lighter when we include super-

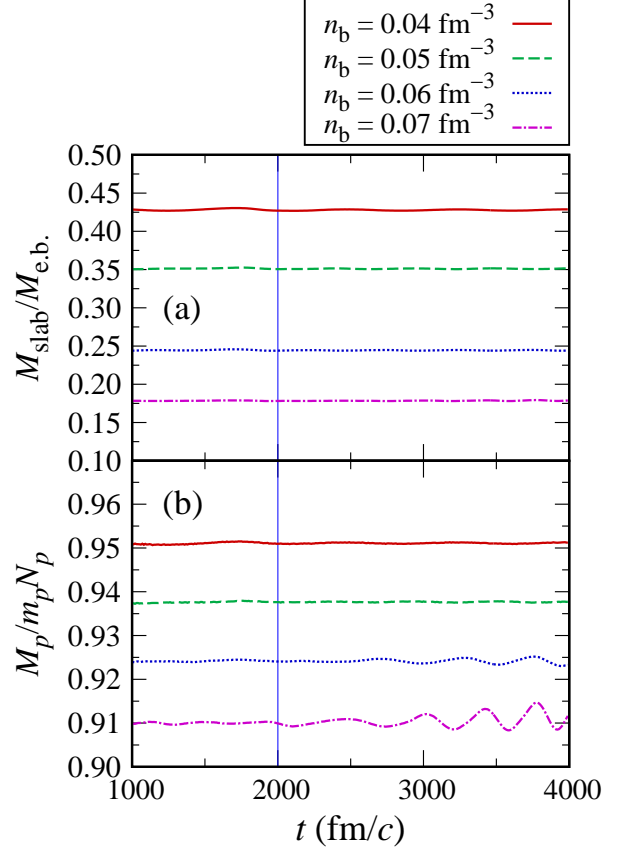


FIG. 7. Results of fully self-consistent time-dependent superfluid band theory calculations for $n_b = 0.04$ (solid line), 0.05 (dashed line), 0.06 (dotted line), and 0.07 fm^{-3} (dash-dotted line) under the β -equilibrium condition. (a) A ratio between the collective mass of the slab and the mass of energetically-bound nucleons, $M_{\text{slab}}/M_{\text{e.b.}}$, is shown as a function of time. (b) A ratio between the collective mass of protons and the total mass of protons, $M_p/m_p N_p$, is shown as a function of time. The vertical line indicates the time up to which the external force is turned on.

fluidity, which means that less neutrons are entrained via band structure effects.

Using those quantities presented in Fig. 6, the collective mass of the slab (70) and that of protons (71) can be deduced. The results are shown in Fig. 7, where the ratio of M_{slab} to the mass of “energetically-bound” neutrons per unit area $M_{\text{e.b.}} \equiv m_p N_p + m_n N_n^{\text{e.b.}}$ are shown in panel (a), and the ratio of M_p to the total mass of protons per unit area $m_p N_p$ are shown in panel (b). The number of “energetically-bound” neutrons, which are within the potential well, is calculated as [19]

$$N_n^{\text{e.b.}} = \frac{1}{N_{k_z}} \sum_{\nu k_z} \int \frac{k_{\parallel}}{\pi} n_{\nu \mathbf{k}}^{(n)} \theta(U_n^0 - e_{\nu \mathbf{k}}^{(n)}) dk_{\parallel}, \quad (76)$$

where $\theta(x)$ is the Heaviside step function, where $\theta(x) = 0$ for $x < 0$ and $\theta(x) = 1$ for $x \geq 0$. $e_{\nu \mathbf{k}}^{(n)}$ denotes single-particle energy after removal of kinetic energy associated with motion

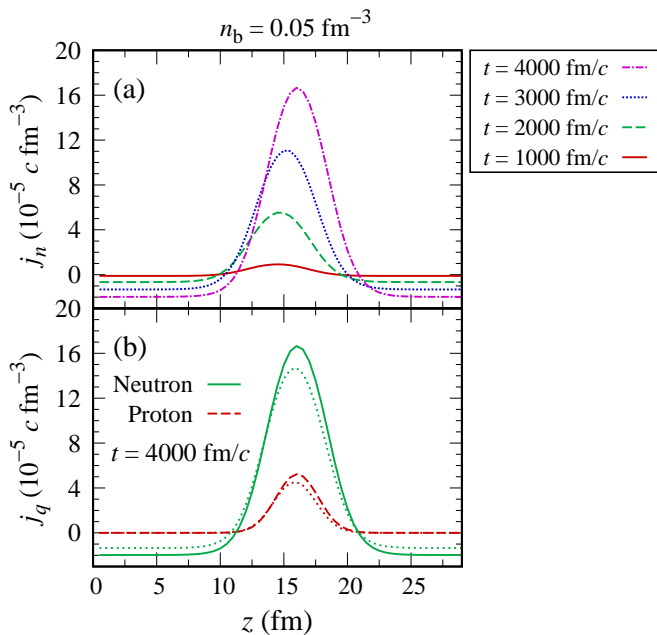


FIG. 8. Results of fully self-consistent time-dependent superfluid band theory calculations for the system with $n_b = 0.05 \text{ fm}^{-3}$ under the β -equilibrium condition. (a) Neutron current density is shown as a function of the z coordinate at four representative instances, $t = 1,000$ (solid line), $2,000$ (dashed line), $3,000$ (dotted line), and $4,000 \text{ fm}/c$ (dash-dotted line). (b) Current densities of neutrons (solid line) and protons (dashed line) are shown at $t = 4,000 \text{ fm}/c$. Results obtained without superfluidity are also shown in (b) by thin dotted lines, for comparison.

parallel to the slabs,

$$e_{\nu\mathbf{k}}^{(n)} \equiv \varepsilon_{\nu\mathbf{k}}^{(n)} - \frac{1}{a} \int_0^a v_{\nu\mathbf{k}}^{(n)*}(z) \frac{\hbar^2 k_{\parallel}^2}{2m_n^{\oplus}(z)} v_{\nu\mathbf{k}}^{(n)}(z) dz. \quad (77)$$

From Fig. 7(b), we see that the collective mass of protons is slightly reduced by about 5–9%. This reduction was already found in the previous work without superfluidity [19], which can be explained by the density-dependent microscopic effective mass. Namely, protons behave as if they have a mass of $m_{p,\text{bg}}^{\oplus} \equiv m_p^{\oplus}[n_{n,\text{b.g.}}]$. In stark contrast, in Fig. 7(a), we find that the collective mass of the slab is significantly *reduced* by about 57.5–82.5% from the naive estimation of energetically-bound neutrons which are within the potential well. Apparently, this significant reduction can not be explained solely by the density-dependent microscopic effective mass of neutrons. Note that if dripped neutrons were actually entrained to the slabs via band structure effects, the collective mass of the slab would be increased. Therefore, this counter-intuitive phenomenon is called the “anti-entrainment” effects [19].

As discussed in the previous work [19], the cause of the reduction can be found in time evolution of current densities. In Fig. 8(a), we show neutron current densities obtained by time-dependent superfluid band theory calculations as a function of z coordinate for the $n_b = 0.05 \text{ fm}^{-3}$ case. The results are shown for four representative instances at $t = 1,000 \text{ fm}/c$ (solid line), $2,000 \text{ fm}/c$ (dashed line), $3,000 \text{ fm}/c$ (dotted line),

TABLE III. Results of fully self-consistent time-dependent band theory calculations with (2nd to 4th columns) and without (5th to 7th columns) superfluidity. The baryon number density n_b is indicated in the first column in fm^{-3} . In the 2nd and 3rd (5th and 6th) columns, free neutron number density n_n^f and conduction neutron number density n_n^c are shown as a ratio to the average neutron number density \bar{n}_n , respectively. In the 4th (7th) column, macroscopic effective mass m_n^* is shown as a ratio to the microscopic effective mass at the background neutron number density $m_{n,\text{bg}}^{\oplus}$, which is calculated with (without) superfluidity.

n_b	Superfluid (TD)DFT			Normal (TD)DFT		
	n_n^f/\bar{n}_n	n_n^c/\bar{n}_n	$m_n^*/m_{n,\text{bg}}^{\oplus}$	n_n^f/\bar{n}_n	n_n^c/\bar{n}_n	$m_n^*/m_{n,\text{bg}}^{\oplus}$
0.04	0.702	0.893	0.785	0.710	0.876	0.810
0.05	0.684	0.913	0.749	0.697	0.896	0.778
0.06	0.609	0.933	0.652	0.608	0.911	0.668
0.07	0.555	0.954	0.582	0.555	0.929	0.598

and $4,000 \text{ fm}/c$ (dash-dotted line). From Fig. 8(a), it is visible that neutrons around the slab (which was initially $z = a/2 = 14.5 \text{ fm}$) move towards the direction of the external force ($+z$ direction), because the current density is positive. On the other hand, the neutron current density outside the slab becomes negative, meaning that those dripped neutrons move towards $-z$ direction, opposite to the external force. Since the presence of the “counterflow” reduces not only the magnitude of the total linear momentum, P_{tot} , but also its rate of increase, \dot{P}_{tot} , it results in the reduction of the collective mass of the slab. One could attribute the emergence of the counterflow to the band structure effects [19]. Namely, since the macroscopic effective mass depends on the second derivative of single-particle energy $\varepsilon_{\nu\mathbf{k}}^{(n)}$ with respect to the Bloch wave number k_z [18, 19], it can be either positive or negative depending on the curvature of the band. Dripped neutrons in the band which is convex upward may have negative macroscopic effective mass, and they respond towards the opposite direction to the external force. Based on the fully self-consistent time-dependent superfluid band theory calculations, here we showed that the anti-entrainment effects do present even with the inclusion of neutron superfluidity.

To examine the role of superfluidity in the anti-entrainment phenomenon, we compare the results with and without superfluidity at $t = 4,000 \text{ fm}/c$ in Fig. 8(b). Normal static and time-dependent band theory calculations were performed for the same system, keeping all computational parameters unchanged. Neutron (proton) current density obtained with superfluid band theory is shown by solid (dashed) line, while those obtained with normal band theory are shown by dotted lines. From Fig. 8(b), we find that the peak values around the slab are slightly larger for the superfluid system, consistent with the larger values of acceleration observed in Fig. 6. In addition, looking at the neutron current density outside of the slab, we find that the counter flow is also enhanced with superfluidity. Those observations suggest that the anti-entrainment effect is slightly enhanced by the inclusion of neutron superfluidity.

From the extracted collective masses shown in Fig. 7, we

can evaluate the conduction neutron number density, n_n^c (74), and the macroscopic effective mass, $m_n^*/m_{n,\text{bg}}^\oplus$ (75). Since the extracted masses slightly fluctuate in time (cf. Fig. 7), we take an average over the time interval, $2,000 \text{ fm}/c \leq t \leq 4,000 \text{ fm}/c$, in which the external force is kept constant. The results are summarized in Table III. In the 2nd to 4th columns, results obtained with superfluidity are shown, while those without superfluidity are also shown in 5th to 7th columns, for comparison. In both cases with and without superfluidity, the conduction neutron number density n_n^c is larger than the ‘free’ neutron number density n_n^f , for all densities examined, $n_b = 0.04\text{--}0.07 \text{ fm}^{-3}$. It means that the band structure actually works like lubricant to mobilize dripped neutrons. As a result, the macroscopic effective mass m_n^* becomes smaller than the microscopic effective mass for background neutron number density $m_{n,\text{bg}}^\oplus$. By comparing 4th and 7th columns, we find that the inclusion of superfluidity slightly enhances the reduction by a few %. It is remarkable that the inclusion of superfluidity does not change the conclusion of Refs. [18, 19], at least for the slab phase of the inner crust of neutron stars.

3. Remarks on other calculations

In this section, we discuss relevance and difference of the present results with other calculations.

First of all, our conclusion of the anti-entrainment in the slab phase looks contradicting to the results of Carter et al. [13], where ordinary entrainment effects were reported with $m_n^*/m_n = 1.02\text{--}1.03$ for $n_b = 0.074\text{--}0.079 \text{ fm}^{-3}$ in the slab phase. We consider that the difference is caused by an improper definition of free neutron number density, as pointed out in Ref. [18]. That is, in the definition of Carter et al. [13], kinetic energy associated with the motion parallel to the slab was involved when they judge if neutrons are below or above the nuclear potential well. Because of this fact, the free neutron number density, n_n^f , is substantially overestimated in the calculations of Ref. [13] that resulted in entrainment effects with larger values of $m_n^*/m_n = n_n^f/n_n^c$. We have actually confirmed that $m_n^*/m_n > 1$ is obtained if we use the definition of Ref. [13], in a similar way as reported in Ref. [18].

Second, in Refs. [33, 34], it is advocated that superfluidity has a strong impact on the entrainment effects and also anti-entrainment effects are absent, which contradict to our conclusion. We point out here that it is mainly caused by different theoretical frameworks and definitions of the effective mass. In Refs. [33, 34], a simple toy model that uses a sinusoidal external potential, which mimics a crystalline structure, was employed. On top of that external potential, band calculations based on BCS- and/or HFB-type theories were performed to quantify the macroscopic effective mass via a standard formula from the band theory of solids. In the simple model of Refs. [33, 34], the effective mass is defined with the *superfluid fraction*, which is inevitably smaller than or equal to the total particle number density of the system under the external potential. It is thus by definition impossible to obtain the anti-entrainment effect in their model. On the contrary in our framework, the effective mass is defined as

the ratio of the number density of *energetically free* neutrons, which are seemingly free from the potential, to the number density of conduction neutrons, which can actually conduct. We note that our fully self-consistent calculations showed that more than 90% of neutrons actually participate in conduction (cf. the 3rd and 6th columns of Table III). It underlines the importance of the self-organizing character of nuclear systems, where neutrons and protons form clusters by themselves through the nucleon-nucleon interaction, and there is no external periodic potential. The latter property is in stark contrast to ordinary solids, where electrons are assumed, to a good approximation, to feel an external periodic potential of an ionic lattice in the sense of the Born-Oppenheimer approximation.

Lastly, it is to mention that we have also examined two static treatments for calculating the neutron effective mass. The first one is the method that was employed in, e.g., Refs. [13, 14, 17–19]. In the latter method, the effective mass is evaluated with the mobility coefficient which is calculated as a sum of inverse effective mass tensors which depend on curvature of each band as a function of the Bloch wave number. The other one is the method that was employed in Ref. [71]. In the latter case, TDSLDA equations are solved in a gauge that simulates induced superflow, and the effective mass of an impurity can be extracted from a static response of the system. With both approaches, we have obtained the results which are qualitatively consistent with our real-time method, indicating the anti-entrainment effects.

Since there remains some room for discussion, such as the definition of free neutrons and the relationship between the superfluid fraction and the conduction neutron number density, we leave quantitative comparisons between those different treatments as a future work.

E. Quasiparticle Resonances

Finally, here we report our complementary finding of an intriguing phenomenon characteristic to superfluid systems, known as *quasiparticle resonances*, in the context of the inner crust of neutron stars and discuss if it is relevant to the entrainment phenomenon.

Usually, quasiparticle resonances are studied in the context of a usual neutron scattering process in a vacuum [72–76]. It is a resonance associated with pairing correlations, where an incoming neutron deposits part of its kinetic energy to the target nucleus, inducing a particle-hole excitation of a bound neutron, and the excited neutron and the incoming one form a Cooper pair which behaves as a resonance. Here we show, within the fully self-consistent superfluid band theory calculations, that quasiparticle resonances do present even in the inner crust of neutron stars, where superfluid neutrons permeate crystalline nuclear matter.

An intuitive way to distinguish quasiparticle resonances among the others is to analyze the occupation probabilities as a function of single-particle energy. However, what we obtain as a solution of the SLDA equation is a set of quasiparticle energies, not the single-particle ones, and one should evaluate the latter in an appropriate manner. In the present work, instead of introducing the canonical basis, we use an alternative

method explained below.

As an effective way to link quasiparticle energies with single-particle ones, we take the following procedure:

1. We solve the SLDA equation self-consistently and obtain quasiparticle energies $E_{\nu\mathbf{k}}^{(q)}$ as well as a set of densities, say, $\rho_{\text{g.s.}}$, and the corresponding single-particle Hamiltonian $h_{\mathbf{k},\text{g.s.}}^{(q)} \equiv h^{(q)}[\rho_{\text{g.s.}}] + h_{\mathbf{k}}^{(q)}[\rho_{\text{g.s.}}]$.
2. Next, we diagonalize the single-particle Hamiltonian $h_{\mathbf{k},\text{g.s.}}^{(q)}$ and obtain ‘effective’ single-particle energies, say, $\check{\varepsilon}_{\nu'\mathbf{k}}^{(q)}$. (Note that we put a breve accent to indicate that they are not necessarily exactly equal to the true single-particle energies, $\varepsilon_{\nu'\mathbf{k}}^{(q)}$.) The indices $\{\nu'\mathbf{k}\}$ are labeling the effective single-particle energies, $\check{\varepsilon}_{\nu'\mathbf{k}}^{(q)}$, in the ascending order.
3. We then evaluate the corresponding quasiparticle energies using the relation,

$$\check{E}_{\nu'\mathbf{k}}^{(q)} = \sqrt{(\check{\varepsilon}_{\nu'\mathbf{k}}^{(q)} - \lambda_q)^2 + \overline{\Delta}_q^2}, \quad (78)$$

where $\overline{\Delta}_q$ represents the average absolute value of the pairing field, defined in Eq. (68).

4. We reorder the obtained quasiparticle energies, $\check{E}_{\nu'\mathbf{k}}^{(q)}$ (78), in the ascending order, $\check{E}_{\nu'\mathbf{k}}^{(q)} \rightarrow \check{E}_{\nu\mathbf{k}}^{(q)}$, where we store the correspondence between the indices, $\{\nu'\mathbf{k}\} \Leftrightarrow \{\nu\mathbf{k}\}$.
5. Based on the following correspondences,

$$\varepsilon_{\nu'\mathbf{k}}^{(q)} \approx \check{\varepsilon}_{\nu'\mathbf{k}}^{(q)} \Leftrightarrow \check{E}_{\nu'\mathbf{k}}^{(q)} \approx E_{\nu\mathbf{k}}^{(q)}, \quad (79)$$

we regard that the single-particle energies $\varepsilon_{\nu'\mathbf{k}}^{(q)}$ are associated with the corresponding states $\{\nu'\mathbf{k}\} \Leftrightarrow \{\nu\mathbf{k}\}$ having occupation probabilities,

$$n_{\nu\mathbf{k}}^{(q)} = \frac{1}{a} \int_0^a |v_{\nu\mathbf{k}}^{(q)}(z)|^2 dz. \quad (80)$$

The estimated quasiparticle energies, $\check{E}_{\nu\mathbf{k}}^{(q)}$ (78), may not exactly be equal to the true ones, $E_{\nu\mathbf{k}}^{(q)}$, but in the most cases we found a good correspondence, $\check{E}_{\nu\mathbf{k}}^{(q)} \simeq E_{\nu\mathbf{k}}^{(q)}$, with a correct ordering of the quasiparticle energies.

In Fig. 9, we show neutron occupation probabilities $n_{\nu\mathbf{k}}^{(n)}$ as a function of single-particle energies $\varepsilon_{\nu'\mathbf{k}}^{(n)}$, calculated for the system with $n_b = 0.05 \text{ fm}^{-3}$ under the β -equilibrium condition, as a typical example. Since single-particle energies are the same for $\pm k_z$, results are plotted for a half of the first Brillouin zone, $0 \leq k_z \leq \pi/a$. The plot is restricted to $k_{\parallel} = 0$ in Fig. 9(a) for better visibility, while occupation probabilities for all states within the plotting range, $-20 \text{ MeV} \leq \varepsilon_{\nu'\mathbf{k}}^{(n)} \leq 40 \text{ MeV}$, are presented in Fig. 9(b).

First, let us focus on the $k_{\parallel} = 0$ case, shown in Fig. 9(a). From the figure, we see that occupation probabilities globally follow a Fermi-Dirac-type distribution, as it should be,

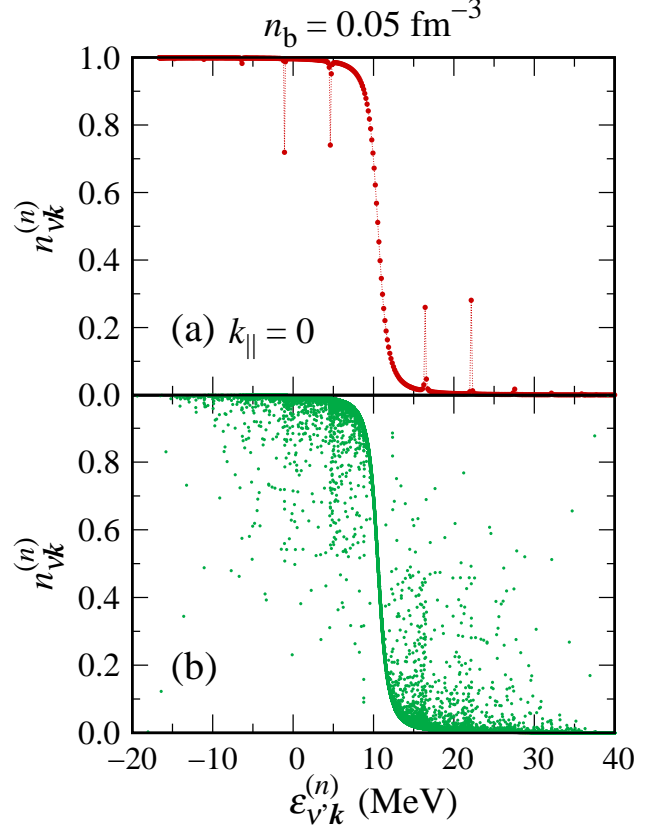


FIG. 9. Occupation probabilities of neutrons, $n_{\nu\mathbf{k}}^{(n)}$, are shown as a function of single-particle energy, $\varepsilon_{\nu'\mathbf{k}}^{(n)}$, for states with $0 \leq k_z \leq \pi/a$ and $n_b = 0.05 \text{ fm}^{-3}$ under the β -equilibrium condition. In panel (a), occupation probabilities are plotted only for states with $k_{\parallel} = 0$ for better visibility, while in panel (b), results are plotted for all states.

indicating that the above mentioned procedure works well. In addition to that, we find that there appear several irregular dips and peaks below and above the chemical potential $\lambda_n \simeq 10.8 \text{ MeV}$, respectively. Clearly, the peaks embedded in the continuum, paired up with the dips in the bound states, manifest the expected characteristic of quasiparticle resonances, that is, they form Cooper pairs to gain pairing energy.

To serve another look at its behavior, we show in Fig. 10(a) single-particle energies of neutrons $\varepsilon_{\nu'\mathbf{k}}^{(n)}$ as a function of the Bloch wave number k_z in the first Brillouin zone, $-\pi/a \leq k_z \leq \pi/a$, with $k_{\parallel} = 0$. In the figure, occupation probabilities are indicated by the opacity of the data symbols. From the figure, we find that the single-particle energies nicely exhibit the expected band structure (cf. Refs. [18, 19]). On top of that, we can clearly see that there are four irregular states above the chemical potential, which sustain noticeable occupation probabilities. A closer look at the results reveals that hole-like states with relatively small occupation probabilities are present at the same k_z below the chemical potential, meaning that Cooper pairs are formed between the states with the same Bloch wave vector \mathbf{k} . We note that these quasiparticle resonances could be observed, thanks to the band theory cal-

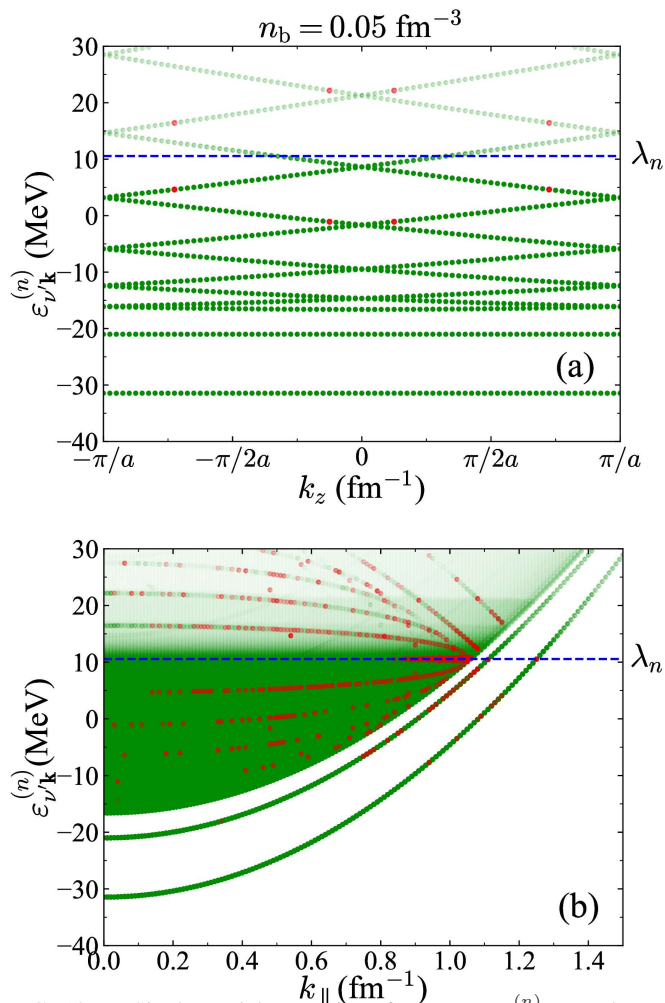


FIG. 10. Single-particle energies of neutrons, $\varepsilon_{\nu'k}^{(n)}$, are shown as functions of k_z for $k_{||} = 0$ (a) and as functions of $k_{||}$ for $0 \leq k_z \leq \pi/a$ (b), for the system with $n_b = 0.05 \text{ fm}^{-3}$ under the β -equilibrium condition. Horizontal dashed line indicates the neutron chemical potential λ_n . Occupation probabilities $n_{\nu'k}^{(n)}$ are represented by opacity of symbols. In both panels, states regarded as quasiparticle resonances are highlighted in red color.

culations, i.e., they are absent for the $k_z = 0$ case, in this particular example. We consider that the essence is a better treatment of the continuum states—the resonances would not be resolved if there were no pairs of states with close values of $|\varepsilon_{\nu'k}^{(n)} - \lambda_n|$ within a resonance width. In addition, we plot in Fig. 10(b) single-particle energies as a function of $k_{||}$ as well. The states regarded as quasiparticle resonances are highlighted by red color. From these figures, we find that pairing is simply associated with single-particle states around the chemical potential. If there were a large band gap ($\Delta\varepsilon > \overline{\Delta}_n$) and the chemical potential were located in between the gap, pairing would have been suppressed. In the slab phase, however, band gaps are only a few to tens of keV [18, 19], which are much smaller than the average absolute value of the pairing field, $\overline{\Delta}_n \approx 1 \text{ MeV}$. Therefore, pairing properties are insensitive to the band structure, in the slab phase under study.

In Fig. 9(b), we show occupation probabilities for all states ($k_z > 0$ and $k_{||} \geq 0$) as a function of single particle energies.

Intriguingly, we find that there are a number of quasiparticle resonances for a range of single-particle energies, as can be seen from the figure. Thus, on top of the usual entrainment effects, where one expects that part of dripped neutrons are effectively immobilized by the periodic potential, there could be an additional contribution from quasiparticle resonances which are detectable only in microscopic superfluid calculations.

To estimate the impact of quasiparticle resonances on the entrainment phenomenon, we calculate the total number of resonating neutrons per unit area, N_n^{res} . N_n^{res} is calculated by integrating densities of states above the chemical potential, but with relatively large occupation probabilities greater than 0.1, that we considered as candidates of the quasiparticle resonances. To exclude the states having $n_{\nu'k}^{(n)} > 0.1$ in the tail of the global Fermi-Dirac-type distribution, only those exhibiting sudden changes of occupation probabilities in neighboring energies are regarded as quasiparticle resonances. The results for various densities, $n_b = 0.04, 0.05, 0.06,$ and 0.07 fm^{-3} , are summarized in Table IV. In the 5th column of Table IV, we show the total number of resonating neutrons per unit area within a single slab period a , N_n^{res} . These numbers should be compared with the expected number of bound neutrons. Here we take a ratio between the number of resonating neutrons to the number of “energetically-bound” neutrons (76), $N_n^{\text{res}}/N_n^{\text{e.b.}}$, and it is listed in the 6th column of Table IV. From the results, we find that the number of resonating neutrons is only less than or around 1% of the number of energetically-bound neutrons in the system. We also find that the number of resonating neutrons decreases as the baryon number density increases. The latter observation can be explained by looking at the change of the potential. In the 2nd, 3rd, and 4th columns of Table IV, the minimum and the maximum values of the mean-field potential, U_n^{min} and U_n^0 , respectively, and the chemical potential, λ_n , are presented. Because more and more neutrons are dripped out of the slabs as the baryon number density increases, the maximum value of the mean-field potential decreases substantially, while the minimum value is not so much affected. It means that the depth of the potential well becomes shallower for higher baryon number densities and, as a result, there are less bound orbitals which can contribute to the quasiparticle resonances. Therefore, although the phenomenon itself is physically intriguing, its impact on the entrainment effect is negligibly small.

V. CONCLUSION AND PROSPECT

In this work, we have developed a fully self-consistent time-dependent superfluid band theory for the inner crust of neutron stars, based on time-dependent density functional theory (TDDFT) extended for superfluid systems, known as time-dependent superfluid local density approximation (TDSLDA). It should be noted that our theoretical framework, though it is yet restricted to 1D slab structure, is much more realistic than other existing models on the market. Namely, our theory is based on the microscopic framework of (TD)DFT, which can correctly describe properties of finite nuclei, not only static

TABLE IV. Results of the SLDA calculations for baryon number densities $n_b = 0.04, 0.05, 0.06, \text{ and } 0.07 \text{ fm}^{-3}$ under the β equilibrium condition are listed in 2nd–5th rows, respectively. From left to right columns, it shows: baryon number density, n_b , in fm^{-3} , the minimum and the maximum values of the mean-field potential, U_n^{min} and U_n^0 , in MeV, the neutron chemical potential, λ_n , in MeV, the number of resonating neutrons per unit area, N_n^{res} , in fm^{-2} , and its ratio to the number of energetically-bound neutrons, $N_n^{\text{res}}/N_n^{\text{e.b.}}$ [cf. Eq. (76)].

n_b	U_n^{min}	U_n^0	λ_n	N_n^{res}	$N_n^{\text{res}}/N_n^{\text{e.b.}}$
0.04	-37.3	-13.1	9.48	1.09×10^{-2}	2.49%
0.05	-37.6	-16.7	10.6	3.92×10^{-3}	0.88%
0.06	-39.4	-20.3	11.6	2.54×10^{-3}	0.36%
0.07	-38.7	-23.8	12.7	1.05×10^{-3}	0.14%

structure, but also excitations and reaction dynamics, as well as nuclear matter properties, in a unified way. We do not *a priori* assume any external potential nor cluster shape, whereas nuclear pasta is formed self-consistently through the effective nucleon-nucleon interaction. By applying the real-time method, where we measure the collective mass of a nuclear cluster immersed in neutron superfluid through a response of the system to an external force, we have successfully extracted the conduction neutron number density and the macroscopic effective mass of dripped neutrons. From the results, we have found that the dripped neutrons are actually mobilized by the band structure, that is, the conduction neutron number density is enhanced and the neutron effective mass is reduced, which we call the *anti-entrainment* effects. These results are consistent with recent self-consistent band calculations without superfluidity [18, 19], that is, no significant qualitative difference was observed in the cases with and without superfluidity. We have demonstrated that the neutron effective mass is substantially reduced up to about 42% in the slab phase and superfluidity slightly enhances this anti-entrainment effect.

As a next step, we have already extended the present formalism to include finite temperature and magnetic field effects (cf. [78]). It enables us to quantify, e.g., the melting temperature of the slabs, taking into account the band structure effects. We expect that such fully self-consistent finite-temperature band theory calculations of nuclear pasta phases in a hot environment will be useful, e.g., for studying supernova matter or cooling of proto-neutron stars. Interesting and useful information such as neutrino-pasta scattering, elastic properties, as well as neutron-star cooling will be obtained in our forthcoming works.

Needless to say, it is highly desired to extend the present work to 2D and 3D geometries. We believe that the formalism itself is unchanged and can be extended to higher dimensions in a straightforward way. Thus, the major obstacle is the computational cost. As we mentioned in Sec. III, we have already dealt with millions of quasiparticle wave functions for the 1D geometry. The extensions to 2D and 3D geometries would require tens to thousands times larger number of quasiparticle orbitals and the number of numerical operations for those lattice points would be increased. To avoid diagonalizations of a

matrix with such a huge dimension, we may take advantage of shifted conjugate-orthogonal conjugate-gradient (COCG) [79] or shifted conjugate-orthogonal conjugate-residual (COCR) [80] methods. These methods allow us to extract various densities by contour integrations, where a shifted algorithm can be used to efficiently evaluate quantities at different points in the complex plane. It has been shown that these methods are particularly suitable to GPU parallelization, since a huge number of operations at different coordinates \mathbf{r} are independent from each other. In addition, TDSLDA has also been shown remarkable successes with the use of top-tier supercomputers working with GPUs [81]. The use of GPUs would enable us to realize fully self-consistent time-dependent superfluid band theory calculations for 2D and 3D geometries and to resolve the controversial situation concerning the entrainment effects in the inner crust of neutron stars.

ACKNOWLEDGMENTS

We are grateful to Takashi Nakatsukasa (University of Tsukuba) and Kenichi Yoshida (RCNP, Osaka University) for valuable discussions. We also thank Giorgio Almirante (IJCLab) for communication that resolved an error in our computational code. Meetings in the A3 Foresight Program supported by JSPS are also acknowledged for useful discussions. One of the authors (K.Y.) would like to acknowledge the support from the Hiki Foundation, Tokyo Institute of Technology. This work mainly used computational resources of the Yukawa-21 supercomputer at Yukawa Institute for Theoretical Physics (YITP), Kyoto University. This work also used (in part) computational resources of the HPCI system (Grand Chariot) provided by Information Initiative Center (IIC), Hokkaido University, through the HPCI System Project (Project ID: hp230180). This work is supported by JSPS Grant-in-Aid for Scientific Research, Grant Nos. 23K03410 and 23K25864.

Appendix A: On total energy per nucleon

As we mentioned in Sec. IV B, slab-period dependence of energy of the system shows different behavior with and without electrons' contribution. In this Appendix, we provide a comparison between those two cases.

In Figs. 11(a)–(d), we present the total energy per nucleon for $n_b = 0.04, 0.05, 0.06, \text{ and } 0.07 \text{ fm}^{-3}$, respectively, under the β -equilibrium condition as a function of the slab period a . The results with electrons' contribution (E_{tot}/A) are shown by filled circles connected with solid lines, while those without electrons' contribution (E_{nucl}/A) are shown by open circles connected with dotted lines. That is, the latter results are the same as those shown in Fig. 3 in the main texts.

From the figure, we find that both energies, E_{tot}/A and E_{nucl}/A , exhibit a parabolic shape which is convex downward as a function of the slab period a . The minimum energy locations are shifted towards larger a values by 12, 11, 2, 2 fm for $n_b = 0.04, 0.05, 0.06, \text{ and } 0.07 \text{ fm}^{-3}$. We find that the shift is

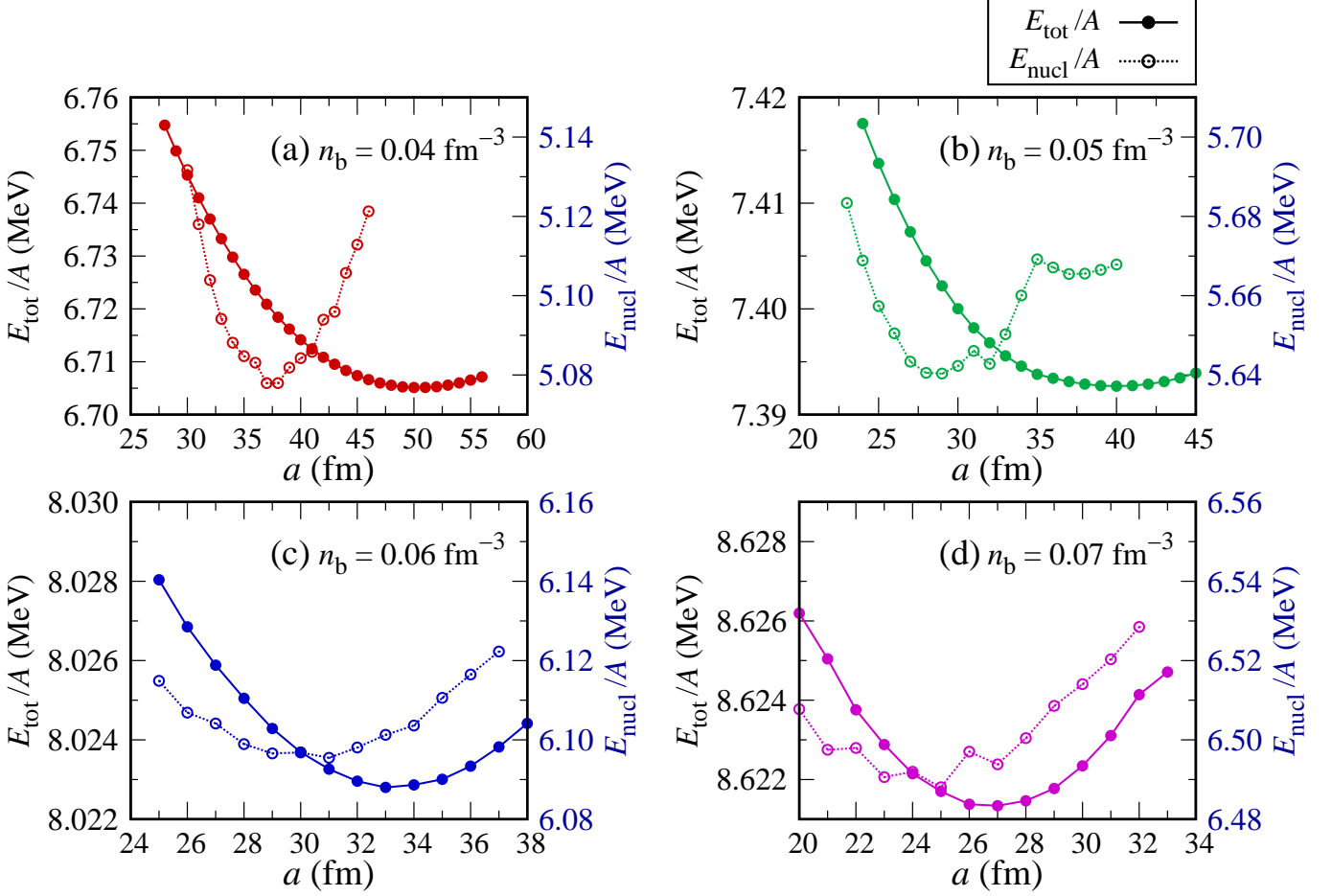


FIG. 11. Energy per nucleon is shown as a function of the slab period a . Total energy per nucleon which include electrons' contribution, E_{tot}/A , is shown by solid circles connected with solid lines, while that without electrons contribution, E_{nucl}/A , is shown by open circles connected with dotted lines. In panels (a)–(d), results obtained for different baryon number densities, $n_b = 0.04, 0.05, 0.06$, and 0.07 fm^{-3} , respectively, under the β -equilibrium condition are presented. Note that left and right vertical axes correspond to E_{tot}/A and E_{nucl}/A , respectively.

smaller for higher density region where emergence of the slab phase is actually expected ($n_b \simeq 0.07\text{--}0.08 \text{ fm}^{-3}$). To obtain an equilibrium configuration of nuclear pasta phases under the β -equilibrium condition, the total energy, rather than the nuclear energy, should be minimized. Because the use of larger

a values (i.e., larger N_z) requires substantial computational effort, and we expect that it will not change the conclusion of the present article, the configurations that minimize the nuclear energies were analyzed in this work.

-
- [1] P. Hohenberg and W. Kohn, Inhomogeneous Electron Gas, *Phys. Rev.* **136**, B864 (1964).
 - [2] W. Kohn and L.J. Sham, Self-Consistent Equations Including Exchange and Correlation Effects, *Phys. Rev.* **140**, A1133 (1965).
 - [3] W. Kohn, Nobel Lecture: Electronic structure of matter—wave functions and density functionals, *Rev. Mod. Phys.* **71**, 1253 (1999).
 - [4] E. Runge and E.K.U. Gross, Density-Functional Theory for Time-Dependent Systems, *Phys. Rev. Lett.* **52** (1984) 997.
 - [5] M.A.L. Marques, C.A. Ullrich, F. Nogueira, A. Rubio, K. Burke, and E.K.U. Gross, *Time-Dependent Density Functional Theory*, *Lect. Notes Phys.* **706** (Springer, Berlin Heidelberg

- berg 2006).
- [6] M.A.L. Marques, N.T. Maitra, F.M.S. Nogueira, and E.K.U. Gross (ed. A. Rubio), *Fundamentals of Time-Dependent Density Functional Theory*, *Lecture Notes in Physics*, Vol. 837 (Springer, Berlin Heidelberg 2012).
- [7] K. Yabana and G.F. Bertsch, Time-dependent local-density approximation in real time, *Phys. Rev. B* **54**, 4484 (1996).
- [8] G.F. Bertsch, J.-I. Iwata, A. Rubio, and K. Yabana, Real-space, real-time method for the dielectric function, *Phys. Rev. B* **62**, 7998 (2000).
- [9] K. Yabana, T. Sugiyama, Y. Shinohara, T. Otobe, and G.F. Bertsch, Time-dependent density functional theory for strong electromagnetic fields in crystalline solids, *Phys. Rev.*

- B **85**, 045134 (2012).
- [10] A. Yamada and K. Yabana, Multiscale time-dependent density functional theory for a unified description of ultrafast dynamics: Pulsed light, electron, and lattice motions in crystalline solids, *Phys. Rev. B* **99**, 245103 (2019).
- [11] X. Andrade, D. Strubbe, U. De Giovannini, A. Hjorth Larsen, M.J.T. Oliveira, J. Alberdi-Rodriguez, A. Varas, I. Theophilou, N. Helbig, M.J. Verstraete, L. Stella, F. Nogueira, A. Aspuru-Guzik, A. Castro, M.A.L. Marques, and A. Rubio, Real-space grids and the Octopus code as tools for the development of new simulation approaches for electronic systems, *Phys. Chem. Chem. Phys.* **17**, 31371 (2015); https://octopus-code.org/wiki/Main_Page.
- [12] M. Noda, S.A. Sato, Y. Hirokawa, M. Uemoto, T. Takeuchi, S. Yamada, A. Yamada, Y. Shinohara, M. Yamaguchi, K. Iida, I. Floss, T. Otake, K.-M. Lee, K. Ishimura, T. Boku, G.F. Bertsch, K. Nobusada, and K. Yabana, SALMON: Scalable Ab-initio Light-Matter simulator for Optics and Nanoscience, *Compt. Phys. Commun.* **235**, 356 (2019); <https://salmon-tddft.jp/>.
- [13] B. Carter, N. Chamel, and P. Haensel, Entrainment coefficient and effective mass for conduction neutrons in neutron star crust: simple microscopic models, *Nucl. Phys.* **A748**, 675 (2005).
- [14] N. Chamel, Band structure effects for dripped neutrons in neutron star crust, *Nucl. Phys.* **A747**, 109 (2005).
- [15] N. Chamel, Effective mass of free neutrons in neutron star crust, *Nucl. Phys.* **A773**, 263 (2006).
- [16] N. Chamel, S. Naimi, E. Khan, and J. Margueron, Validity of the Wigner-Seitz approximation in neutron star crust, *Phys. Rev. C* **75**, 055806 (2007).
- [17] N. Chamel, Neutron conduction in the inner crust of a neutron star in the framework of the band theory of solids, *Phys. Rev. C* **85**, 035801 (2012).
- [18] Yu Kashiwaba and T. Nakatsukasa, Self-consistent band calculations of the slab phase in the neutron-star crust, *Phys. Rev. C* **100**, 035804 (2019).
- [19] K. Sekizawa, S. Kobayashi, and M. Matsuo, Time-dependent extension of the self-consistent band theory for neutron star matter: Anti-entrainment effects in the slab phase, *Phys. Rev. C* **105**, 045807 (2022).
- [20] K. Oyamatsu and Y. Yamada, Shell energies of non-spherical nuclei in the inner crust of a neutron star, *Nucl. Phys.* **A578**, 184 (1994).
- [21] M. Onsi, A.K. Dutta, H. Chatri, S. Goriely, N. Chamel, and J.M. Pearson, Semi-classical equation of state and specific-heat expressions with proton shell corrections for the inner crust of a neutron star, *Phys. Rev. C* **77**, 065805 (2008).
- [22] N. Chamel, Entrainment in Superfluid Neutron-Star Crusts: Hydrodynamic Description and Microscopic Origin, *J. Low Temp. Phys.* **189**, 328 (2017).
- [23] N. Andersson, K. Glampedakis, W.C.G. Ho, and C.M. Espinoza, Pulsar Glitches: The Crust is not Enough, *Phys. Rev. Lett.* **109**, 241103 (2012).
- [24] N. Chamel, Crustal Entrainment and Pulsar Glitches, *Phys. Rev. Lett.* **110**, 011101 (2013).
- [25] B. Haskell and A. Melatos, Models of pulsar glitches, *Int. J. Mod. Phys. D* **24**, 153008 (2015).
- [26] N. Chamel, J. Margueron, and E. Khan, Neutron specific heat in the crust of neutron stars from the nuclear band theory, *Phys. Rev. C* **79**, 012801(R) (2009).
- [27] N. Chamel, D. Page, and S. Reddy, Low-energy collective excitations in the neutron star inner crust, *Phys. Rev. C* **87**, 035803 (2013).
- [28] K. Kobyakov and C.J. Pethick, Dynamics of the inner crust of neutron stars: Hydrodynamics, elasticity, and collective modes, *Phys. Rev. C* **87**, 055803 (2013).
- [29] K. Kobyakov and C.J. Pethick, Nucleus-nucleus interactions in the inner crust of neutron stars, *Phys. Rev. C* **94**, 055806 (2016).
- [30] D. Durel and M. Urban, Long-wavelength phonons in the crystalline and pasta phases of neutron-star crusts, *Phys. Rev. C* **97**, 065805 (2018).
- [31] J.A. Sauls, N. Chamel, and M.A. Alpar, Superfluidity in Disordered Neutron Star Crust, arXiv:2001.09959 [astro-ph.HE].
- [32] B. Carter, N. Chamel, and P. Haensel, Effects of BCS pairing on entrainment in neutron superfluid current in neutron star crust, *Nucl. Phys.* **A759**, 441 (2005).
- [33] G. Watanabe and C.J. Pethick, Superfluid Density of Neutrons in the Inner Crust of Neutron Stars: New Life for Pulsar Glitch Models, *Phys. Rev. Lett.* **119**, 062701 (2017).
- [34] Y. Minami and G. Watanabe, Effects of pairing gap and band gap on superfluid density in the inner crust of neutron stars, *Phys. Rev. Research* **4**, 033141 (2022).
- [35] A. Bulgac, P. Magierski, and M.M. Forbes, *The Unitary Fermi Gas: From Monte Carlo to Density Functionals*, in: BCS-BEC Crossover and the Unitary Fermi Gas (ed.) W. Zwerger; Lecture Notes in Physics, Vol. **836**, pp. 305–373 (Springer, Heidelberg, 2012).
- [36] A. Bulgac, Time-Dependent Density Functional Theory for Fermionic Superfluids: From Cold Atomic Gases–To Nuclei and Neutron Stars Crust, *Phys. Status Solidi B* **256**, 1800592 (2019).
- [37] L.N. Oliveira, E.K.U. Gross, and W. Kohn, Density-Functional Theory for Superconductors, *Phys. Rev. Lett.* **60**, 2430 (1988).
- [38] O.-J. Wacker, R. Kümmel, and E.K.U. Gross, Time-Dependent Density-Functional Theory for Superconductors, *Phys. Rev. Lett.* **73**, 2915 (1994).
- [39] S. Kurth, M. Marques, M. Lüders, and E.K.U. Gross, Local Density Approximation for Superconductors, *Phys. Rev. Lett.* **83**, 2628 (1999).
- [40] A. Bulgac and Y. Yu, Renormalization of the Hartree-Fock-Bogoliubov Equations in the Case of a Zero Range Pairing Interaction, *Phys. Rev. Lett.* **88**, 042504 (2002).
- [41] A. Bulgac, Local density approximation for systems with pairing correlations, *Phys. Rev. C* **65**, 051305(R) (2002).
- [42] A. Bulgac and S. Yoon, Large Amplitude Dynamics of the Pairing Correlations in a Unitary Fermi Gas, *Phys. Rev. Lett.* **102**, 085302 (2009).
- [43] A. Bulgac, Y.-L. Luo, P. Magierski, K.J. Roche, and Y. Yu, Real-Time Dynamics of Quantized Vortices in a Unitary Fermi Superfluid, *Science* **332**, 1288 (2011).
- [44] M. Bender, P.-H. Heenen, and P.-G. Reinhard, Self-consistent mean-field models for nuclear structure, *Rev. Mod. Phys.* **75**, 121 (2003).
- [45] C. Simenel, Nuclear quantum many-body dynamics, *Eur. Phys. J. A* **48**, 152 (2012).
- [46] T. Nakatsukasa, K. Matsuyanagi, M. Matsuo, and K. Yabana, Time-dependent density-functional description of nuclear dynamics, *Rev. Mod. Phys.* **88**, 045004 (2016).
- [47] C. Simenel and A.S. Umar, Heavy-ion collisions and fission dynamics with the time-dependent Hartree-Fock theory and its extensions, *Prog. Part. Nucl. Phys.* **103**, 19 (2018).
- [48] P.D. Stevenson and M.C. Barton, Low-energy heavy-ion reactions and the Skyrme effective interaction, *Prog. Part. Nucl. Phys.* **104**, 142 (2019).
- [49] K. Sekizawa, TDHF Theory and Its Extensions for Multinucleon Transfer Reactions: A Mini Review, *Front. Phys.* **7**, 20 (2019).
- [50] A. Bulgac, P. Magierski, K.J. Roche, and I. Stetcu, Induced

- Fission of ^{240}Pu within a Real-Time Microscopic Framework, Phys. Rev. Lett. **116**, 122504 (2016).
- [51] G. Wlazłowski, K. Sekizawa, P. Magierski, A. Bulgac, and M.M. Forbes, Vortex Pinning and Dynamics in the Neutron Star Crust, Phys. Rev. Lett. **117**, 232701 (2016).
- [52] P. Magierski, K. Sekizawa, and G. Wlazłowski, Novel Role of Superfluidity in Low-Energy Nuclear Reactions, Phys. Rev. Lett. **119**, 042501 (2017).
- [53] A. Bulgac, S. Jin, K.J. Roche, N. Schunck, and I. Stetcu, Fission dynamics of ^{240}Pu from saddle to scission and beyond, Phys. Rev. C **100**, 034615 (2019).
- [54] P. Magierski, A. Makowski, M.C. Barton, K. Sekizawa, and G. Wlazłowski, Pairing dynamics and solitonic excitations in collisions of medium-mass, identical nuclei, Phys. Rev. C **105**, 064602 (2022).
- [55] A. Bulgac, M.M. Forbes, M.M. Kelley, K.J. Roche, and G. Wlazłowski, Quantized Superfluid Vortex Rings in the Unitary Fermi Gas, Phys. Rev. Lett. **112**, 025301 (2014).
- [56] G. Wlazłowski, A. Bulgac, M.M. Forbes, and K.J. Roche, Life cycle of superfluid vortices and quantum turbulence in the unitary Fermi gas, Phys. Rev. A **91**, 031602(R) (2015).
- [57] G. Wlazłowski, K. Sekizawa, M. Marchwiany, and P. Magierski, Suppressed Solitonic Cascade in Spin-Imbalanced Superfluid Fermi Gas, Phys. Rev. Lett. **120**, 253002 (2018).
- [58] K. Hossain, K. Kobuszewski, M.M. Forbes, P. Magierski, K. Sekizawa, and G. Wlazłowski, Rotating Quantum Turbulence in the Unitary Fermi Gas, Phys. Rev. A **105**, 013304 (2022).
- [59] B. Tüzemen, T. Zawiślak, G. Wlazłowski, P. Magierski, Disordered structures in ultracold spin-imbalanced Fermi gas, New J. Phys. **25**, 033013 (2023).
- [60] A. Barresi, A. Boulet, P. Magierski, and G. Wlazłowski, Dissipative Dynamics of Quantum Vortices in Fermionic Superfluid Phys. Rev. Lett. **130**, 043001 (2023).
- [61] N.W. Ashcroft, N.D. Mermin, and D. Wei, *Solid State Physics Revised Edition* (Cengage Learning Asia Pte Ltd, 2016).
- [62] N. Martin and M. Urban, Superfluid hydrodynamics in the inner crust of neutron stars, Phys. Rev. C **94**, 065801 (2016).
- [63] D.G. Ravenhall, C.J. Pethick, and J.R. Wilson, Structure of Matter below Nuclear Saturation Density, Phys. Rev. Lett. **50**, 2066 (1983).
- [64] M. Hashimoto, H. Seki, and M. Yamada, Shape of Nuclei in the Crust of Neutron Star, Prog. Theor. Phys. **71**, 320 (1984).
- [65] P.W. Anderson and N. Itoh, Pulsar glitches and restlessness as a hard superfluidity phenomenon, Nature **256**, 25 (1975).
- [66] P.W. Anderson, Infrared Catastrophe in Fermi Gases with Local Scattering Potentials, Phys. Rev. Lett. **18**, 1049 (1967).
- [67] T. Lesinski, M. Bender, K. Bennaceur, T. Duguet, and J. Meyer, Tensor part of the Skyrme energy density functional: Spherical nuclei, Phys. Rev. C **76**, 014312 (2007).
- [68] M. Kortelainen, R.J. Furnstahl, W. Nazarewicz, and M.V. Stoitsov, Natural units for nuclear energy density functional theory, Phys. Rev. C **82**, 011304(R) (2010).
- [69] E. Chabanat, P. Bonche, P. Haensel, J. Meyer, and R. Schaeffer, A Skyrme parametrization from subnuclear to neutron star densities Part II. Nuclei far from stabilities, Nucl. Phys. **A635**, 231 (1998); **A643**, 441 (1998).
- [70] A. Baran, A. Bulgac, M.M. Forbes, G. Hagen, W. Nazarewicz, N. Schunck, and M.V. Stoitsov, Broyden's method in nuclear structure calculations, Phys. Rev. C **78**, 014318 (2008).
- [71] P. Magierski, B. Tüzemen, and G. Wlazłowski, Dynamics of spin-polarized impurity in ultracold Fermi gas, Phys. Rev. A **104**, 033304 (2021).
- [72] J. Dobaczewski, W. Nazarewicz, T.R. Werner, J.F. Berger, C.R. Chinn, and J. Dechargé, Mean-field description of ground-state properties of drip-line nuclei: Pairing and continuum effects, Phys. Rev. C **53**, 2809 (1996).
- [73] K. Bennaceur, J. Dobaczewski, and M. Płoszajczak, Continuum effects for the mean-field and pairing properties of weakly bound nuclei, Phys. Rev. C **60**, 034308 (1999).
- [74] A. Bulgac, Hartree-Fock-Bogoliubov Approximation for Finite Systems, arXiv:nucl-th/9907088.
- [75] Y. Kobayashi and M. Matsuo, Effects of pairing correlation on the low-lying quasiparticle resonance in neutron drip-line nuclei, Prog. Theor. Exp. Phys. **2016**, 013D01 (2016).
- [76] Y. Kobayashi and M. Matsuo, *s*-wave quasiparticle resonance in neutron-rich drip-line nuclei, Prog. Theor. Exp. Phys. **2020**, 013D03 (2020).
- [77] P. Papakonstantinou, J. Margueron, F. Gulminelli, and Ad.R. Raduta, Densities and energies of nuclei in dilute matter at zero temperature, Phys. Rev. C **88**, 045805 (2013).
- [78] K. Sekizawa and K. Yoshimura, Time-Dependent Superfluid Band Theory for the Inner Crust of Neutron Stars: Current Status and Future Challenges, arXiv:2310.06411 [nucl-th].
- [79] S. Jin, A. Bulgac, K. Roche, and G. Wlazłowski, Coordinate-space solver for superfluid many-fermion systems with the shifted conjugate-orthogonal conjugate-gradient method, Phys. Rev. C **95**, 044302 (2017).
- [80] Y. Kashiwaba and T. Nakatsukasa, Coordinate-space solver for finite-temperature Hartree-Fock-Bogoliubov calculations using the shifted Krylov method, Phys. Rev. C **101**, 045804 (2020).
- [81] S. Jin, K.J. Roche, I. Stetcu, I. Abdurrahman, and A. Bulgac, The LISE package: Solvers for static and time-dependent superfluid local density approximation equations in three dimensions, Comput. Phys. Commun. **269**, 108130 (2021).
- [82] A. Bulgac and Y. Yu, Renormalization of the Hartree-Fock-Bogoliubov Equations in the Case of a Zero Range Pairing Interaction, Phys. Rev. Lett. **88**, 042504 (2002).
- [83] Y. Yu and A. Bulgac, Energy Density Functional Approach to Superfluid Nuclei, Phys. Rev. Lett. **90**, 222501 (2003).
- [84] A. Bulgac, M.M. Forbes, S. Jin, R.N. Perez, and N. Schunck, Minimal nuclear energy density functional, Phys. Rev. C **97**, 044313 (2018).
- [85] See supplemental material of: G. Wlazłowski, K. Sekizawa, P. Magierski, A. Bulgac, and M.M. Forbes, Vortex Pinning and Dynamics in the Neutron Star Crust, Phys. Rev. Lett. **117**, 232701 (2016).
- [86] T. Okihashi and M. Matsuo, Proximity effect of pair correlation in the inner crust of neutron stars, Prog. Theor. Exp. Phys. **2021**, 023D03 (2021).